Life Cycle Evolution of Inhomogeneous Mixing in Shallow Cumulus Clouds

Jung-Sub Lim[1], **Fabian Hoffmann**[1]

[1]Meteorological Institute, Ludwig Maximilian University of Munich, Munich, Germany.

Key Points:

- The evolution of predominant mixing scenarios during the shallow cumulus life cycle is investigated
- While homogeneous mixing is prevalent, inhomogeneous mixing gradually increases as the cloud ages
- Inhomogeneous mixing is more favored for higher aerosol concentrations and in drier boundary layers

Corresponding author: Fabian Hoffmann, fa.hoffmann@lmu.de

Abstract

Understanding how entrainment and mixing shape the cloud droplet size distribution (DSD) is crucial for understanding the optical properties and precipitation efficiency of clouds. Different mixing scenarios, mainly homogeneous and inhomogeneous, shape the DSD in a distinct way and alter the cloud's impact on climate. However, the prevalence of these mixing scenarios and how they vary in space and time is still uncertain, as underlying processes are commonly unresolved by conventional numerical models. To overcome this challenge, we employ the L^3 model, which considers supersaturation fluctuations and turbulent mixing down to the finest relevant lengthscales, making it possible to represent different mixing scenarios realistically. We investigate the spatial and temporal evolution of mixing scenarios over the life cycle of shallow cumulus clouds for varying boundary layer humidities and aerosol concentrations. Our findings suggest homogeneous mixing is generally predominant in cumulus clouds, while different mixing scenarios occur concurrently in the same cloud. Notably, inhomogeneous mixing increases over the cloud life cycle across all analyzed cases. The mean and standard deviation of supersaturation are found to be the most capable indicators of this evolution, providing a comprehensive insight into the characteristics of mixing scenarios. Finally, we show inhomogeneous mixing is more prevalent in drier boundary layers and for higher aerosol concentrations, underscoring the need for a more comprehensive investigation of how these mixing dynamics evolve in a changing climate.

Plain Language Summary

Clouds play a crucial role in Earth's climate system by influencing the radiation balance and moisture transfer. When clouds mix with their environment, a process known as entrainment and mixing, the number and size of cloud droplets change, affecting cloud optical properties and their ability to precipitate. This mixing can happen in two major ways: either the cloud and environmental air are well-mixed (homogeneous mixing) or unevenly mixed (inhomogeneous mixing). However, accurately representing these effects, particularly inhomogeneous mixing, is challenging in weather or climate models, as essential scales and processes are unresolved. By applying a high-resolution model, we investigate how mixing scenarios evolve over the cloud life cycle. We show that while homogeneous mixing prevails, older (mature or dissipating) clouds tend to mix more inhomogeneously. Moreover, clouds in drier and more polluted environments are shown to favor inhomogeneous mixing. In these environments, inhomogeneous mixing becomes the predominant mixing scenario for older clouds, emphasizing the need for further investigations on the impact of different mixing scenarios in a changing climate.

1 Introduction

The role of clouds in the climate system and their representation in climate models remains a significant uncertainty (Boucher et al., 2013; Forster et al., 2021). Entrainment and mixing are among the most perplexing yet vital processes affecting the optical properties and precipitation efficiency of clouds by shaping the cloud droplet size distribution (DSD). While the concept of extreme mixing scenarios, namely homogeneous and inhomogeneous, has been introduced a few decades ago (Baker et al., 1980a; Blyth, 1993), there are ongoing discussions regarding the prevalence of specific mixing scenarios – whether each occurs predominantly at the top, or lateral edges of a cloud, how it varies during the cloud life cycle, or how environmental properties shape the mixing type (Burnet & Brenguier, 2007; Lehmann et al., 2009; Jarecka et al., 2013; Schmeissner et al., 2015; Hoffmann et al., 2019; Yeom et al., 2021; Desai et al., 2021; Gao et al., 2021; Hoffmann, 2023; Liu et al., 2023; Yeom et al., 2023).

In theory, the Damköhler number, defined as the ratio between the timescales for turbulent mixing (τ_{mix}) and the microphysical response (τ_{micro}), could be used to determine mixing scenarios (Baker & Latham, 1979; Baker et al., 1980b; Lehmann et al., 2009; Tölle

& Krueger, 2014). τ_{micro} quantifies the speed of droplet evaporation in the entrained air, and one example is the evaporation time scale (Lehmann et al., 2009; Jarecka et al., 2013; Tölle & Krueger, 2014), $\tau_{\text{evap}} = r_v^2(-GS_{\text{e}})^{-1}$, where $S_{\text{e}} < 0$ is the supersaturation of the entrained air and the growth parameter G summarizes the effects of vapor diffusion and heat conduction on droplet evaporation (Yau & Rogers, 1996). On the other hand, $\tau_{\text{mix}} = \left(l^2/\varepsilon\right)^{1/3}$ estimates how fast entrained air is homogenized with cloudy air by turbulent mixing, where l is the lengthscale of a scalar inhomogeneity, such as the entrained air inside the cloud, that breaks down to the Kolmogorov lengthscale through turbulent motions characterized by a turbulence kinetic energy dissipation rate ε.

When the turbulent mixing is faster than the microphysical response ($\tau_{\text{mix}} \ll \tau_{\text{micro}}$), homogeneous mixing dominates, and all droplets experience the same subsaturation and partially evaporate without reducing the cloud droplet number concentration (N_{c}). When the turbulent mixing is slower than the microphysical response ($\tau_{\text{micro}} \ll \tau_{\text{mix}}$), inhomogeneous mixing is expected, and only those droplets exposed to the entrained air are assumed to evaporate completely, resulting in a decrease in N_{c} while the mean droplet size remains constant. A third mixing scenario occurs when the DSD contains numerous small droplets or droplets ascent during mixing. In this case, the mean droplet radius increases by the complete evaporation of the smallest droplets, which narrows the DSD (Krueger et al., 2008; Luo et al., 2022; Lim & Hoffmann, 2023). Thus, each mixing scenario shapes the DSD in a distinct way.

However, conventional models commonly fail to represent these distinct ways and assume homogeneous mixing on all unresolved scales, although it has been argued that homogeneous mixing only dominates on the lengthscale below a few decimeters (Baker et al., 1980b; Lehmann et al., 2009). Such assumption can misrepresent DSD shape changes during mixing, with commensurate effects on cloud optical properties (Chosson et al., 2007; Slawinska et al., 2008; Hill et al., 2009; Xu et al., 2022), as well as the generation of precipitation (Hoffmann et al., 2019). While early studies suggested inhomogeneous mixing had a negligible effect on cloud optical properties (Hill et al., 2009), recent research indicates it can reduce the cloud optical depth by up to 5% in stratocumulus clouds (Xu et al., 2022). This indicates the need for mixing parameterizations that adjust cloud microphysics based on the prevailing mixing scenario.

Early studies attempted to parameterize mixing scenarios using a predetermined parameter, adjusting N_{c} based on an assumed mixing scenario (Morrison & Grabowski, 2008; Hill et al., 2009). This approach, however, assumes a single mixing scenario for all clouds, ignoring the possibility of multiple mixing scenarios occurring concurrently in the same cloud. In recent years, studies focused on investigating the relationship between mixing scenarios and various cloud properties (Tölle & Krueger, 2014; Pinsky et al., 2016; Luo et al., 2020, 2021, 2022; Lim & Hoffmann, 2023), leading to parameterizations that adapt to cloud properties interactively (Xu et al., 2022). Thus, it is essential to gain comprehensive insights into how mixing scenarios vary spatiotemporally and to identify the cloud properties and environmental factors that influence this variability.

Still, examining mixing scenario characteristics is challenging due to the lack of models representing all relevant scales of entrainment and mixing. In this study, we employ the L^3 model, a large eddy simulation (LES) model coupled with a Lagrangian cloud model (LCM) and the linear eddy model (LEM), which allows to explicitly represent LES sub-grid scale mixing on scales as small as a few centimeters (Hoffmann & Feingold, 2019; Hoffmann et al., 2019). This approach was found capable of considering and classifying different mixing scenarios in a single cumulus congestus cloud (Lim & Hoffmann, 2023). This study aims to extend our understanding of the aforementioned three mixing scenarios by investigating how these change in the life cycle of shallow cumulus clouds, developing naturally from a maritime boundary layer.

Cumulus clouds exhibit distinct life cycles, which include developing, mature, and dissipating stages, each with distinct dynamical and microphysical characteristics (Grinnell et al., 1996; Zhao & Austin, 2005; Katzwinkel et al., 2014). Although inhomogeneous mixing is less prevalent in cumulus clouds compared to weakly turbulent stratocumulus clouds (Jarecka et al., 2013; Hoffmann et al., 2019), observational evidence suggests that the predominant mixing type might change over the cloud life cycle (Lehmann et al., 2009; Schmeissner et al., 2015). Therefore, investigating the life cycle dependency of mixing scenarios provides ample opportunities to elucidate the relationship between mixing scenarios, environmental conditions, and microphysical parameters that may be applicable beyond cumulus clouds. In addition to investigating the effect of the internal variability over the cloud life cycle on mixing scenarios, we investigate how varying aerosol concentrations and boundary layer humidities affect these dynamics.

Therefore, this study aims at deepening our understanding of mixing scenario dynamics, including:

- Classifying various mixing scenarios within a single cumulus cloud.
- Investigating how mixing scenarios evolve over the cloud life cycle.
- Identifying which microphysical property or environmental condition affects these changes most.

This paper is structured as follows. Section 2 presents the L^3 model framework, simulation settings, and the method used to determine the cloud life stages. Section 3 shows the changes in the predominant mixing scenario type and the concurrent cloud properties over the cloud life cycle. Section 4 compares the vertical distribution of these properties under different aerosol concentrations and boundary layer humidities. Finally, we conclude our paper in Sec. 5.

2 Model and Simulation

2.1 The L^3 model

This study uses the L^3 model, the LES-LCM-LEM coupled model, representing supersaturation fluctuations and turbulent mixing on the LES sub-grid scale (SGS) (Hoffmann et al., 2019). The dynamical core of our simulations is the System for Atmospheric Modeling (SAM) by Khairoutdinov and Randall (2003), a nonhydrostatic, anelastic LES model.

The LCM models cloud microphysical processes employing individually simulated computational particles, LCM particles or "superdroplets" as in Shima et al. (2009), where each particle represents a group of identical hydrometeors with the same properties, such as liquid radius and aerosol mass. In the L^3 model, the absolute supersaturation fluctuation (δ') of a virtual air volume around each LCM particle that deviates from the LES-resolved absolute supersaturation, $\bar{\delta} = \bar{q_v} - q_s(\bar{T}, p)$, is stored and updated throughout the particle growth history. Here, $\bar{q_v}$ is the LES water vapor mixing ratio, and q_s is the saturation vapor mixing ratio calculated from the LES absolute temperature $\bar{T}$ and hydrostatic pressure p. Thus, the diffusional growth of cloud droplets in L^3 is not only determined by $\bar{\delta}$ but also by δ', which is primarily determined by the LEM.

δ' is redistributed among the LCM particles located in the same LES grid box by the LEM, an explicit turbulence and mixing model developed by Kerstein (1988). In the LEM, the LCM particles in the same LES grid box are arranged in a virtual one-dimensional array, with each LCM particle representing one LEM grid box. The LEM grid size is determined by dividing the LES vertical grid size by the number of LCM particles in the LES grid box. Segments are randomly chosen from this one-dimensional array and internally rearranged to mimic turbulent compression and folding using the so-called triplet map (Kerstein, 1988; Krueger et al., 1997), which is applied with a frequency determined by the LES SGS tur-

bulence intensity. Interested readers are referred to Hoffmann et al. (2019), Hoffmann and Feingold (2019), and Lim and Hoffmann (2023) for details on the L^3 model.

2.2 Simulation

A maritime shallow-cumulus-topped boundary layer is simulated based on the Barbados Oceanographic and Meteorological Experiment (BOMEX) LES intercomparison case (Siebesma et al., 2003). The simulations are initialized with constant heat and moisture fluxes of 8×10^{-3} K m s^{-1} and 5.2×10^{-5} m s^{-1}, respectively. The total model domain is 5.12 km $\times$ 5.12 km $\times$ 2.56 km in x, y, and z directions with isotropic 40 m grid spacing. The model time step Δt is 1 s, and the total model integration time is 9 h. The results are analyzed only for the last 6 h of each simulation.

In each grid box, 100 computational particles are initialized as sea salt (NaCl) aerosol particles. Each particle represents the same number of real aerosol particles or droplets. This number of computational particles ensures 40 cm LEM resolution, corresponding to the typical transition length scale from inhomogeneous to homogeneous mixing (Lehmann et al., 2009), as noted in Lim and Hoffmann (2023). In other words, all relevant scales of inhomogeneous mixing are resolved. Aerosols are initialized with two log-normal distributions, having number concentrations of 118 and 11 cm^{-3} (in total 129 cm^{-3}), geometric mean radii of $r_\mathrm{m} = 19$ and 56 nm and geometric standard deviations of $\sigma_\mathrm{r} = 3.3$ and 1.6, respectively (Derksen et al., 2009). To investigate the effect of different aerosol number concentrations, we simulate three additional aerosol concentrations by halving (64.5 cm^{-3}), doubling (258 cm^{-3}), and quadrupling (516 cm^{-3}) the number concentrations of each mode. For simplicity, halved aerosol concentration cases are referred to as the 64 cm^{-3} cases. The initial dry aerosol radii are randomly generated by following the log-normal distribution parameters given above, and the corresponding equilibrium wet radii of each aerosol are determined by considering the initial ambient humidity. Sedimentation and collision-coalescence processes are not considered as the simulated clouds are assessed to barely precipitate, especially when the initial aerosol concentration exceeds 64.5 cm^{-3}.

In addition to the standard BOMEX configuration (i.e., control boundary layer humidity), two different initial vapor mixing ratio profiles are used: one with a drier and another with a moister boundary layer to investigate the effects of boundary layer humidity. For this purpose, we employ two additional moisture profiles, one with a higher and the other with a lower water vapor mixing ratio q_v ($\pm$0.9 g kg^{-1}) within the cloud layer (Fig. 1a), as in Drueke et al. (2020). In this study, the simulation without modifying the initial q_v profile and with the aerosol concentration of 129 cm^{-3} is referred to as the "control case".

2.3 Cloud Clock for Shallow Cumulus Cloud Life Cycle Classification

Individual clouds are detected as three-dimensional volumes from snapshots of the cloud field. Every 60 s, cloudy grid boxes are identified if their liquid water mixing ratio $q_\mathrm{c} \geq 0.01$ g kg^{-1}. Then, all adjacent cloudy grid boxes are considered to belong to the same cloud. This study considers only clouds consisting of ten or more grid boxes for analysis, and approximately 20 - 30 individual clouds matching these conditions are detected in each snapshot (cf. Fig. 1b).

We apply the 'cloud clock' by Witte et al. (2014) to classify the cloud life stage. The 'cloud clock' uses two variables. First, the cloud-volume-averaged total water mixing ratio (q_t) normalized by the corresponding sub-cloud mixed layer value,

$$q_\mathrm{t}^* = \frac{q_\mathrm{t}}{q_\mathrm{t,ml}}, \tag{1}$$

with the prescribed mixed layer $q_\mathrm{t,ml} = 17.0$ g kg^{-1}. Second, the cloud-volume-averaged potential virtual temperature perturbation,

$$\Delta\theta_\mathrm{v} = \theta_\mathrm{v,c} - \overline{\theta_\mathrm{v,clr}}, \tag{2}$$

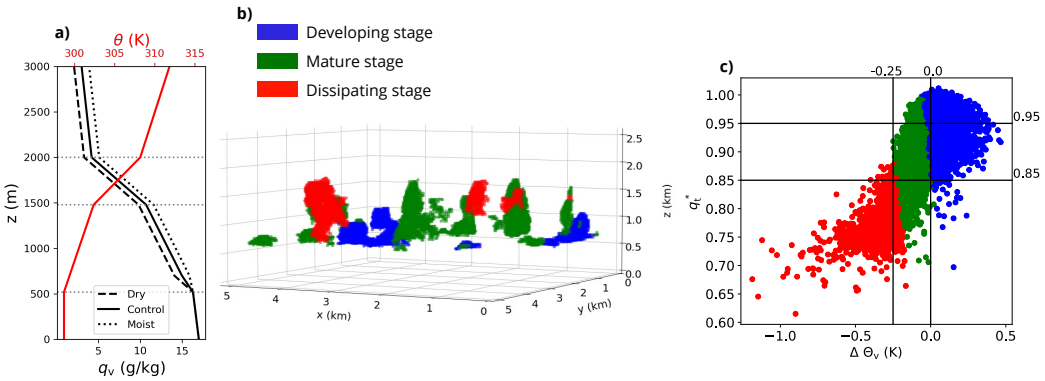

Figure 1. a) Initial potential temperature (red solid line) and vapor mixing ratio profiles for three environmental conditions used in the simulations (black solid line: the control case, dash-dotted line: moister case, and dotted line: drier case). b) An overview of clouds from the control case, color-coded according to their classified life cycle stages at t = 529 min. c) Distributions of the 'cloud clock' variables q_t^* and $\Delta\theta_v$ from each single cloud, for the control case. Different colors in b) and c) indicate different life stages (blue: developing, green: mature, and blue: dissipating)

is used. Here, $\Delta\theta_v$ is calculated from the difference between the in-cloud virtual potential temperature ($\theta_{v,c}$) and the horizontal mean non-cloudy or clear sky value of θ_v, at the same level ($\overline{\theta_{v,clr}}$). Witte et al. (2014) suggested that in shallow cumulus cloud fields, a single-pulsed cloud with $q_t^* > 0.9$ and $\Delta\theta_v > 0$ can be classified as "developing", $q_t^* < 0.85$ and $\Delta\theta_v < 0$ as "dissipating stage", and remaining cases as an intermediate or mature stage.

In this study, shallow cumulus clouds in moister and drier boundary layers are analyzed, potentially changing $q_{t,ml}$. To find appropriate limits to identify life stages, we use K-means clustering by training q_t^* and $\Delta\theta_v$ instead of following the aforementioned criteria by Witte et al. (2014). Interestingly, the K-means clustering classification aligns well with their criteria but is more sensitive to $\Delta\theta_v$ (Fig. 1c).

K-means clustering criteria defines developing clouds by $\Delta\theta_v > 0$ with $q_t^* > 0.85$, dissipating clouds by $\Delta\theta_v < -0.25$ with $q_t^* < 0.85$, and mature clouds for other cases (Fig. 1c). For drier and moister cases, q_t^* values are changed while its differences in each stage and $\Delta\theta_v$ criteria are consistent. Note that this study does not separate potentially multi-pulsed clouds affecting both q_t^* and $\Delta\theta_v$ (Heus et al., 2009; Witte et al., 2014). For the control case, approximately 4,000 clouds are classified to be in the developing stage, 3,000 in the mature stage, and 1,500 in the dissipating stage from 360 snapshots (example for at t = 529 min is shown in Fig. 1b).

3 Evolution of Cloud and Mixing Scenarios

Figure 2 shows the general characteristics of the different simulated cases. The imposed changes in the initial cloud layer q_v (> 500 m) result in a drier or moister sub-cloud layer due to the mixing between two layers (Fig. 2a), while the potential temperature θ barely varies between the simulated cases (Fig. 2b). ε is higher when the boundary layer is moister, especially at the cloud top, due to the higher cloud fraction (f_c) stimulating more turbulence production in this region (Fig. 2c and d). Overall, more clouds are formed in the moister boundary layer and reach higher depths (Fig. 2d and e). Different initial aerosol concentrations primarily affect N_c (Fig. 2f). In drier boundary layers, the lower q_c for almost the same f_c (especially at 1000 m) indicates more dilution by entrainment and mixing (Fig. 2e).

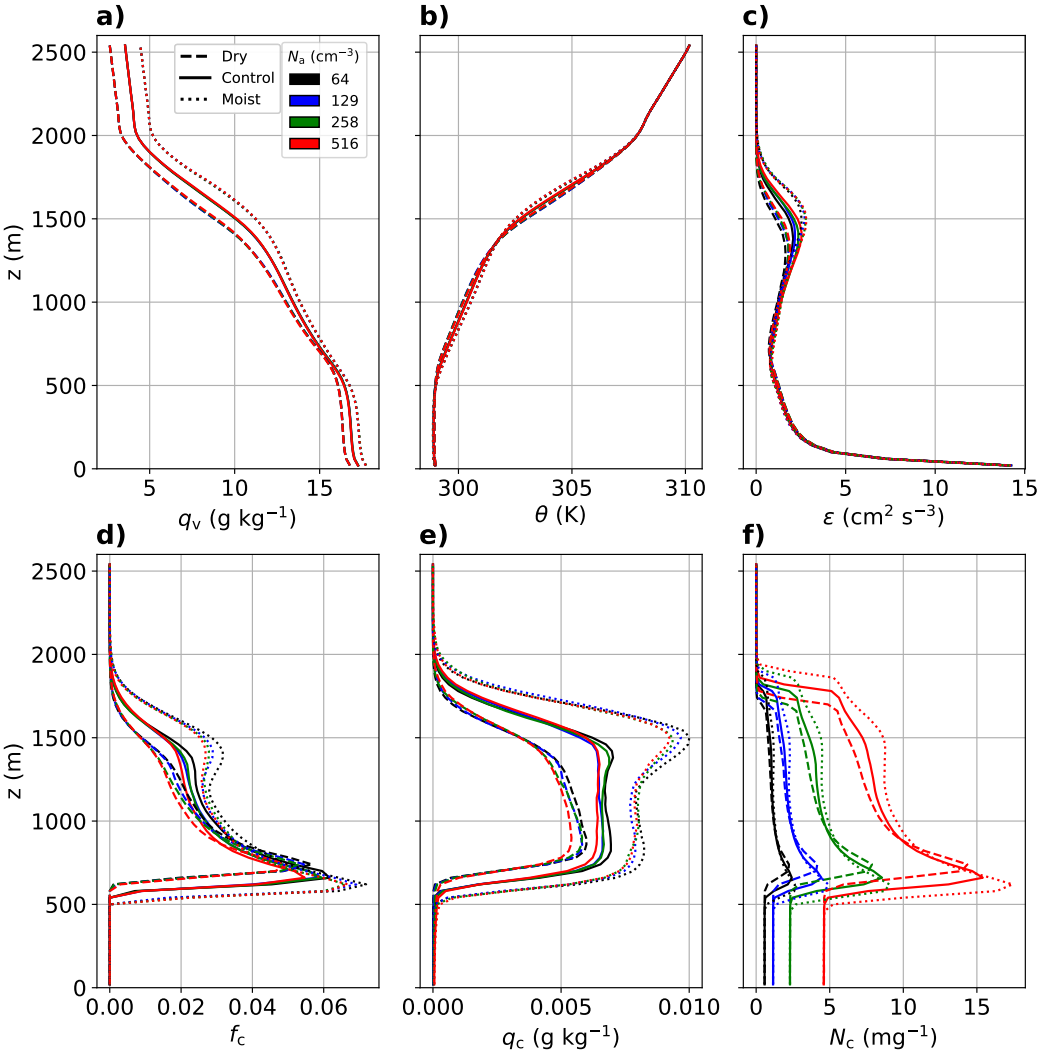

Figure 2. Vertical profiles of a) vapor mixing ratio (q_v), b) potential temperature (θ), c) dissipation rate (ε), d) cloud fraction (f_c), e) cloud water mixing ratio (q_c), f) cloud droplet number concentration (N_c). The line colors indicate different initial aerosol concentrations (black: 64 cm^{-3}, blue: 129 cm^{-3}, green: 258 cm^{-3}, and red: 516 cm^{-3}). Line style depicts the cases with different boundary layer humidity (solid: control boundary layer, dashed: drier boundary layer, and dotted: moister boundary layer). Results are averaged over the last six hours of the simulation.

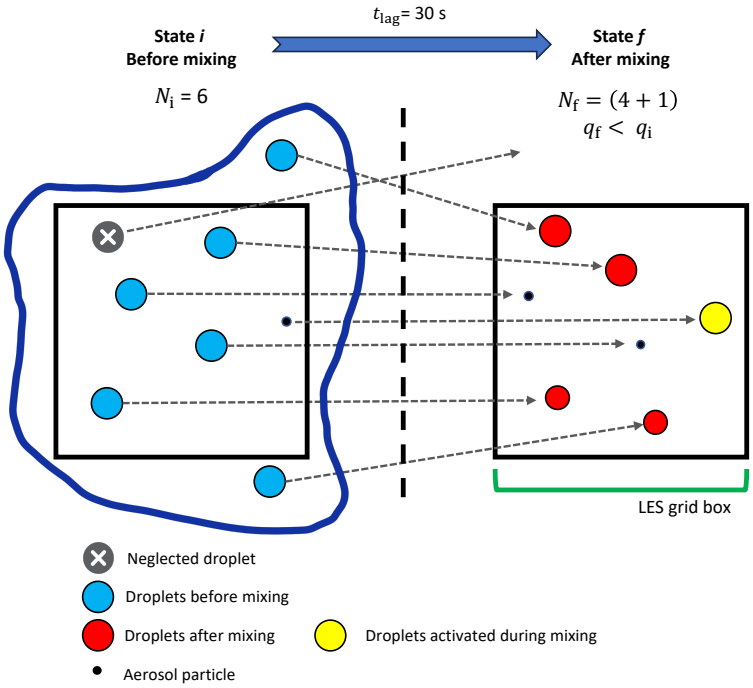

Figure 3. Illustration on the IHMD estimation. Properties of LCM particles before mixing (state i) are estimated by backtracking the particles in the same grid box in state f. The IHMD is estimated from the particles in state f by comparing them to their properties in state i.

3.1 Inhomogeneous Mixing Degree Relative Frequency

Within clouds, different mixing scenarios take place in different locations at the same time. Therefore, it is essential to have a method to quantify the predominant mixing scenario. To classify the mixing scenario in an LES grid box, we use the inhomogeneous mixing degree,

$$\mathrm{IHMD} = \frac{\ln\left(N_{c,f}/N_{c,i}\right)}{\ln\left(q_{c,f}/q_{c,i}\right)}, \tag{3}$$

defined in Lim and Hoffmann (2023), a parameter based on the conceptual cloud microphysical changes for idealized mixing scenarios (Andrejczuk et al., 2006; Morrison & Grabowski, 2008). The IHMD is estimated based on the changes in N_c and q_c before and after mixing, denoted by the subscript i and f, respectively. In extreme homogeneous cases (IHMD = 0), N_c remains constant while q_c decreases, implying the partial evaporation of droplets. In extreme inhomogeneous mixing scenarios (IHMD = 1), N_c changes proportionally to q_c, implying the complete evaporation of droplets. When IHMD is over 1, a decrease in N_c overwhelms the decrease in q_c, resulting in an increase in the droplet mean volume radius due to the complete evaporation of small droplets.

The IHMD is determined by tracking LCM particle properties over a 30 s timelag (t_{lag}) between the before (i) and after (f) mixing state. The IHMD is estimated in regions where mixing occurs defined by $q_{c,f}/q_{c,i} < 0.9$, while both $q_{c,i}$ and $q_{c,f}$ are required to be larger than 0.01 g kg^{-1}. In addition, the LCM mean supersaturation before mixing $\overline{S_i} = \sum_{n=1}^{N_p} S_{i,n}/N_p < -0.05$ to ensure that subsequent changes are driven by entrained air. Here, $S_{i,n} = (\bar{\delta}_i + \delta'_{i,n})/q_s$, where the subscript n denotes the index of individual LCM particle and N_p represents the total number of LCM particles within the same LES grid box at state f. Properties before mixing, such as $q_{c,i}$ and $\overline{S}$ are estimated by backtracking all particles in the

same grid box at the state f. Thus, the particles in state i are not necessarily in the same grid box, and droplets not residing in the grid box at state f are not included in state i property estimation (cf. the neglected droplet in Fig. 3). Note, however, that the particles tend to have similar growth histories for $t_{\mathrm{lag}} = 30$ s (Lim & Hoffmann, 2023).

Both N_{c} and q_{c} typically decrease during entrainment and mixing by dilution and evaporation. However, it is possible that entrained aerosol particles activate during mixing (so-called secondary activation), leading to an increase in $N_{\mathrm{c,f}}$ and potentially $q_{\mathrm{c,f}}$ (Krueger et al., 2008; Chen et al., 2020; Chandrakar et al., 2021). This study incorporates this effect by considering the increased $N_{\mathrm{c,f}}$ and $q_{\mathrm{c,f}}$ (cf. the yellow droplet in Fig. 3). Incorporating secondary activation makes the IHMD smaller (Fig. S1a), primarily by increasing $N_{\mathrm{c,f}}$, counterbalancing a possible decrease in droplet number by complete evaporation. Nevertheless, the overall change in IHMD is negligible (Fig. S1a), as secondary activation is rare (Fig. S1b), potentially due to the aforementioned supersaturation restriction to under -0.05 before mixing. More detailed explanations on IHMD estimation can be found in Sec. 3 of Lim and Hoffmann (2023).

To determine the predominant mixing type of a cloud, IHMDs are classified as one of three major mixing types. Homogeneous mixing is associated where $0 \leq \mathrm{IHMD} < 0.5$ and inhomogeneous mixing where $0.5 \leq \mathrm{IHMD} \leq 1$ considering all intermediate mixing scenarios. Narrowing mixing is associated with $1 < \mathrm{IHMD} \leq 5$. In extreme cases, IHMD can exceed 5, but approximately 98 % of the IHMDs are smaller than this threshold and not included in the estimation. Subsequently, the relative frequency of each mixing scenario, the *mixing scenario relative frequency*,

$$\mathrm{MSRF_X} = n_{\mathrm{X}}/n, \tag{4}$$

is determined, where n is the number of all mixing events in the cloud and n_{X} is the number of all classified homogeneous, inhomogeneous, or narrowing mixing events depending on subscript X. For instance, out of ten mixing events in the entire cloud, six are classified homogeneous, three inhomogeneous, and one narrowing. These values correspond to $\mathrm{MSRF_X}$ of 0.6, 0.3, and 0.1, respectively. Thus, $\mathrm{MSRF_X}$ is beneficial to determine the predominant mixing type in a cloud (e.g., homogeneous in this example), as other mixing scenarios also occur in the same cloud at the same time, while the average of the IHMDs could be biased by potentially large IHMDs during narrowing mixing.

Figure 4a shows the $\mathrm{MSRF_X}$ of each scenario in each cloud as a violin plot for the control case. Each data point represents the value from an individual cloud in the indicated life stage. The homogeneous mixing scenario is the most dominant, and the narrowing mixing scenario is rare throughout the cloud life cycle. Most importantly, the inhomogeneous mixing scenario becomes more frequent as the cloud ages while the dominance of homogeneous mixing decreases commensurately, confirming observational evidence (e.g., Lehmann et al., 2009; Schmeissner et al., 2015).

Results from all simulated cases consistently indicate a trend towards increased inhomogeneous mixing as the cloud ages regardless of the initial conditions (Fig. 4b, c and d). The increase in $\mathrm{MSRF_I}$ from the developing to dissipating stage remains approximately the same for all simulated cases, suggesting a universality in the evolution of inhomogeneous mixing throughout the cumulus cloud life cycle.

The $\mathrm{MSRF_H}$ in developing clouds are over 0.5 for all simulated cases and generally decrease by about 0.1 toward the dissipating stages (Fig. 4b), while the $\mathrm{MSRF_I}$ increases by 0.1 between the developing and dissipating stages. Notably, for the dry boundary layer with the highest aerosol number concentration ($N_{\mathrm{a}} = 516$ cm^{-3}), inhomogeneous mixing is more frequent than homogeneous mixing in the dissipating stage (Fig. 4b and c). Meanwhile, $\mathrm{MSRF_N}$ slightly increases as the cloud ages, but this change is relatively small, with less than 0.02 (see Fig.4d).

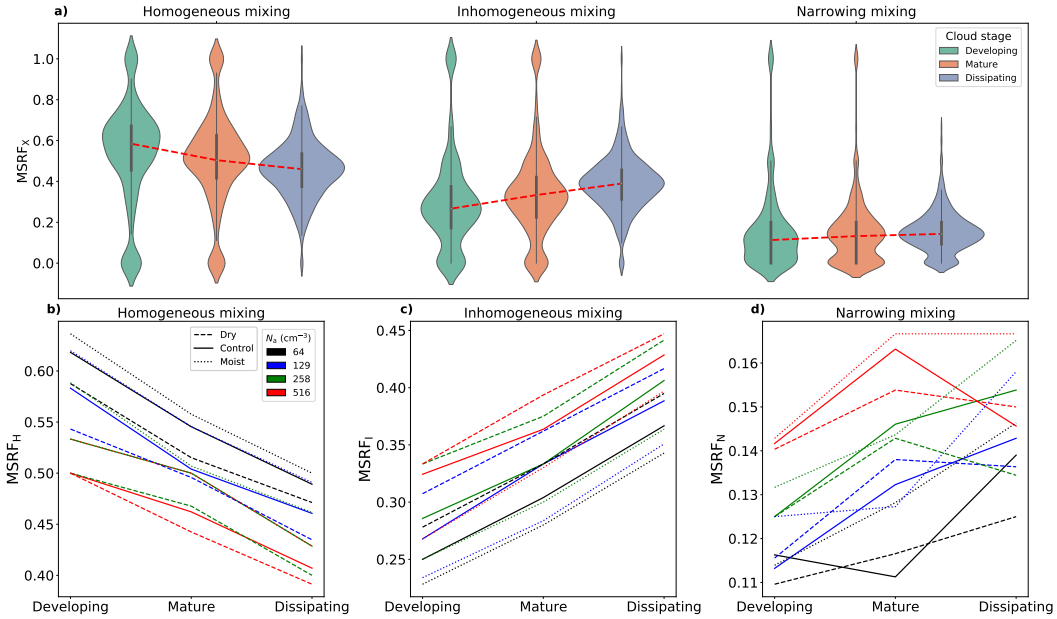

Figure 4. a) Distribution of $MSRF_X$ (homogeneous, inhomogeneous, and narrowing) from individual clouds over different cloud life cycles (developing, mature, and dissipating) for the control case. Mixing scenario medians are connected with red dotted lines to highlight the life cycle changes. The median $MSRF_X$ for b) homogeneous, c) inhomogeneous, and d) narrowing mixing in individual clouds as a function of the cloud life stage (developing, mature, and dissipating) are shown for all simulated cases. The solid line depicts the control case, the dashed line depicts the drier case, and the dotted line indicates the moister case. The colors of the line indicate different initial aerosol number concentrations (black: 64 cm^{-3}, blue: 129 cm^{-3}, green: 258 cm^{-3} and red: 516 cm^{-3}).

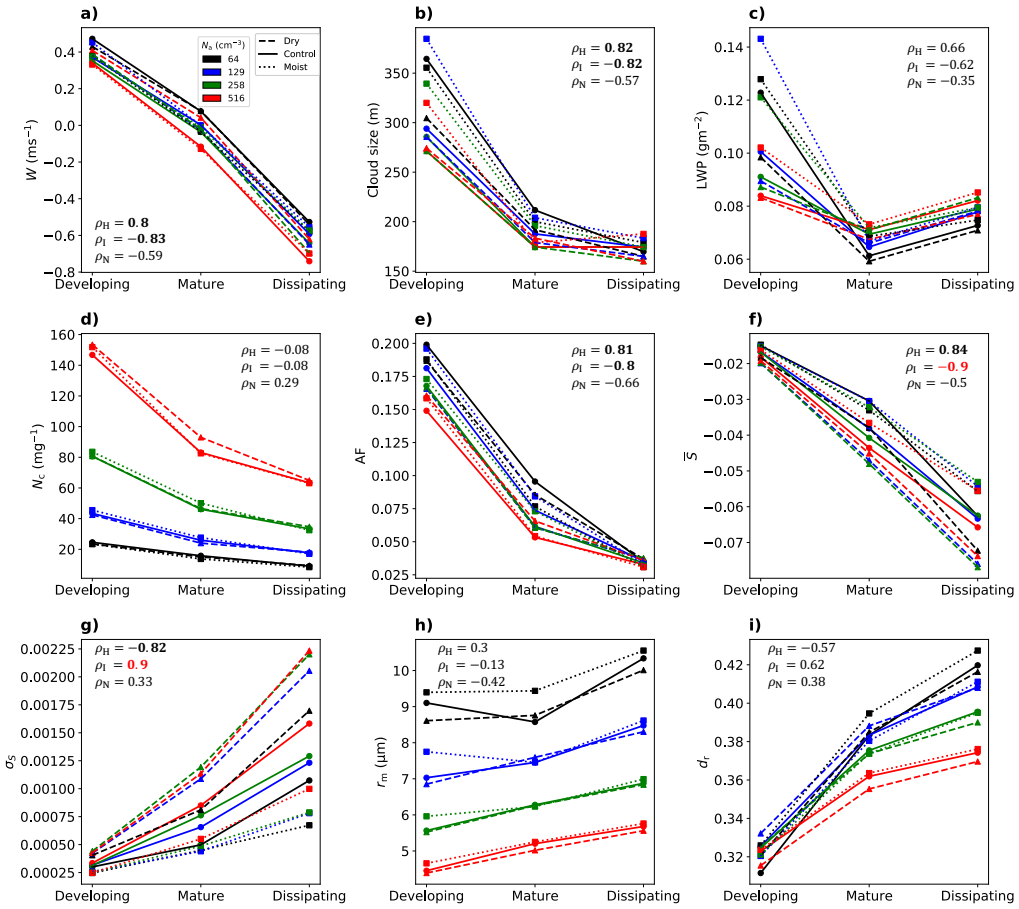

Figure 5. Distributions of cloud volume-averaged median a) vertical velocity (W), b) typical cloud size, c) liquid water path (LWP), d) cloud droplet number concentration (N_c), e) adiabatic fraction (AF), f) mean supersaturation ($\overline{S}$), g) standard deviation of supersaturation (σ_S), h) droplet mean radius (r_m), and i) droplet radius relative dispersion (d_r) for different cloud life stages. The solid line and circle marker indicate the results obtained from cases with control boundary layer humidity. The dashed line and triangle marker indicate the result obtained from a case with a drier boundary layer. The dotted line and square marker denote the results of a case with a moister boundary layer. The colors distinguish cases with different initial aerosol number concentrations. In each panel, the correlation coefficients (ρ_X) with respect to MSRF$_X$ (homogeneous, inhomogeneous, and narrowing) are indicated.

3.2 The Evolution of Cloud-Volume-Averaged Properties over the Life Cycle

To investigate how inhomogeneous mixing evolves, we illustrate the properties related to entrainment and mixing averaged across the entire volume of individual clouds, as represented by:

$$\overline{\phi}_{\text{cloud}} = \frac{1}{V_{\text{cloud}}} \int_{V_{\text{cloud}}} \phi \, dV, \tag{5}$$

where V_{cloud} is the total cloud volume and ϕ is cloud property of interest, such as ε or N_c. Figure 5 shows the median of $\overline{\phi}_{\text{cloud}}$ from individual clouds in different life stages. For clarity, we omit the overbar and subscript in the following.

Over the cloud life cycle, clouds become less buoyant, and their mean vertical velocity (W) decreases similarly in all cases (Fig. 5a). The typical cloud size, determined from the

square root of vertically projected cloudy area (e.g., Neggers et al., 2003), decreases over the life cycle (Fig. 5b). The liquid water path (LWP) also decreases toward the mature stage and remains almost constant afterward (Fig. 5c). In Fig. S2, we show that when considering only clouds larger than 300 m in cloud size, the cloud size increases from the developing to the mature stage and decreases in the dissipating stage. Concurrently, the LWP increases toward the dissipating stage due to the expected large number of deeper clouds toward the end of the cloud life cycle. Other variables barely change if analyzed clouds are constrained to larger cloud sizes.

Figure 5e shows the adiabatic fraction (AF), a ratio between the LWC and the adiabatic LWC at the corresponding level, indicating the degree of cloud dilution (Eytan et al., 2021). As clouds age, clouds are diluted by mixing with environmental air, which decreases AF. Generally, AF decreases similarly over the cloud life cycle in all cases. However, AFs are smaller in more polluted cases, where entrainment is typically stronger (Wang et al., 2003). We should note that values shown in Fig. 5 are averaged over the entire cloud volume, affected by extremely low AFs at the cloud edge (McFarlane & Grabowski, 2007).

The cloud dilution causes a decrease in the mean supersaturation $\overline{S}$ experienced by the LCM particles and an increase in its standard deviation (σ_S) during the cloud life cycle (Fig. 5f and g). More dilution and a lower environmental $\overline{S}$ in the drier boundary layer cases leads to a more substantial decrease in $\overline{S}$. Additionally, the lower $\overline{S}$ in the cases with higher aerosol concentration supports the aforementioned stronger entrainment. Thus, more dilution in the drier and polluted boundary layer cases leads to a higher σ_S (Fig. 5g). This indicates a more inhomogeneous mixture of S in the cloud, a prerequisite for increasing inhomogeneous mixing on the cloud edges.

Dilution also decreases N_c over the cloud life cycle, while the initial aerosol number concentration strongly determines N_c (Fig. 5d). The droplet mean radius increases over the cloud life cycle (Fig. 5h), while droplet size variance increases more due to continuous entrainment and mixing, allowing the droplet size relative dispersion d_r, the ratio between the mean and standard deviation of the droplet radius, to increase over the cloud life cycle (Fig. 5i). The increase in d_r supports the slight increase in narrowing mixing over the cloud life cycle (Fig. 4d). Note that the increase in narrowing mixing is balanced by the decreasing W (Fig. 5a), which prevents further narrowing by lifting (Lim & Hoffmann, 2023).

Overall, cloud-averaged properties and $\mathrm{MSRF_X}$ exhibit consistent changes over the cloud life cycle, regardless of the aerosol concentration and boundary layer humidity (Figs. 4, and 5). We now briefly discuss the correlation of median values ρ_X, shown in Fig. 5. ρ_X is estimated with 36 sets of median values (12 simulated cases and three mixing stages) for $\mathrm{MSRF_X}$ (Fig. 4b, c, and d) and the properties shown in Fig. 5. A complete correlation matrix can be found in Fig. S3.

For $\mathrm{MSRF_I}$, $\overline{S}$ shows the strongest negative correlation (-0.9), alongside the cloud clock variables (q_t^* and $\Delta\theta_v$, as indicated in Fig. S3). On the other hand, σ_S shows the strongest positive correlation with $\mathrm{MSRF_I}$ (0.9), while other properties such as W, cloud size, and AF show a negative correlation around -0.8.

For $\mathrm{MSRF_H}$, correlations are generally lower. The same variables show an inverse relationship compared to $\mathrm{MSRF_I}$ as expected. Maximum correlation is 0.87 for $\Delta\theta_v$, while others range from 0.8 to 0.87. For $\mathrm{MSRF_H}$ and $\mathrm{MSRF_I}$, other properties (LWP, d_r, r_m and N_c) show weak correlations under ±0.6.

The correlations are even weaker for $\mathrm{MSRF_N}$. Here, AF shows the strongest correlation of -0.66, followed by W, q_t^*, cloud size, $\Delta\theta_v$ and $\overline{S}$ with correlations ranging from -0.5 to -0.6. Interestingly, the DSD shape-related parameters, such as d_r and r_m show higher positive (0.38) and negative (-0.42) correlation than σ_S (0.33), suggesting a distinct underlying process for narrowing mixing, in contrast to other two scenarios.

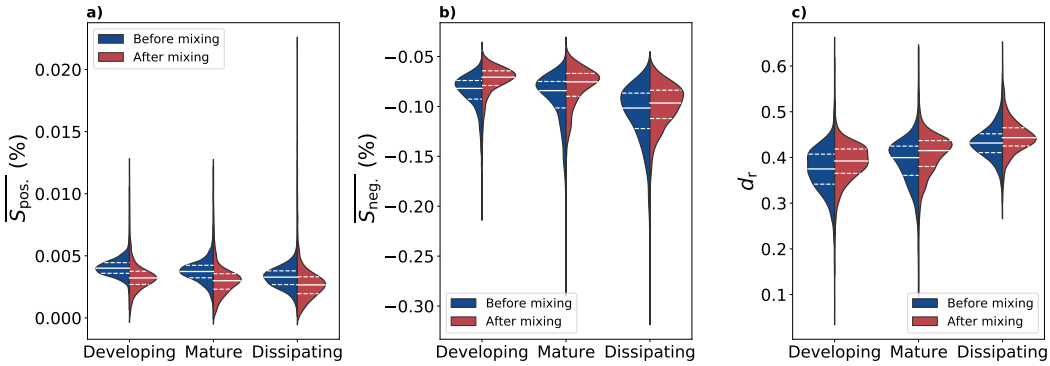

Figure 6. Distributions of mixing region volume-averaged a) mean supersaturation of droplets in supersaturated air, b) mean supersaturation of droplets in subsaturated air, c) droplet radius relative dispersion during mixing. The blue violin plot on the left side of each panel depicts values before mixing, and the red violin plot on the right side depicts values after mixing. All data are obtained from the control case.

This correlation analysis shows that homogeneous and inhomogeneous mixing evolution is highly affected by the $\overline{S}$ and σ_S changes over the cloud life cycle apart from the expected strong correlation with cloud clock variables. It is noteworthy that correlation among the values mentioned above (q_t^*, $\Delta\theta_v$, $\overline{S}$, σ_S, W, cloud size, and AF) are also strong (Fig. S3), indicating the complex interactions of these variables over the cloud life cycle.

3.3 Mixing Region Properties Change During Cloud Life Cycle

The properties averaged over the entire cloud volume provide a valuable overview of how cloud properties change over the cloud life cycle. However, entrainment and mixing occur at the cloud edge, and the properties in this region may differ from those averaged over the entire cloud volume. Thus, it is also important to discuss the properties before and after mixing in the regions where entrainment and mixing occur (Fig. 6).

To distinguish the entrained and cloudy air properties during a mixing event, we assume that subsaturated particles are affected by the entrained air, whereas air unaffected by entrainment remains supersaturated. By using the supersaturation around each LCM particle, we define the average S of supersaturated droplets as $\overline{S_{pos.}}$ and the average S of subsaturated droplets as $\overline{S_{neg.}}$. As expected, $\overline{S_{pos.}}$ decreases and $\overline{S_{neg.}}$ increase during mixing at any cloud life stage (Fig. 6a and b).

Over the cloud life cycle, $\overline{S_{pos.}}$ decreases slightly, and $\overline{S_{neg.}}$ decreases substantially (Fig. 6b). Moreover, $\overline{S_{neg.}}$ after mixing decreases as the cloud ages. This indicates that clouds in the mature and dissipating stages have lower $\overline{S}$, primarily due to the remnants of the entrained air without full restoration of $\overline{S}$ inside the cloud (Fig. 5e). Additionally, the lower $\overline{S}$ inside mature and dissipating clouds may be caused by the lower $\overline{S}$ of the entrained air in these stages. We will discuss this further in Sec. 4.2. Regardless of its origin, stronger subsaturations decrease τ_{micro}, which creates more favorable conditions for inhomogeneous mixing scenarios as the cloud ages.

In the mixing region, d_r generally increases over the cloud life cycle (Fig. 6c). Lim and Hoffmann (2023) showed that in the homogeneous mixing scenarios, d_r increases after mixing, whereas d_r barely changes or even decreases in the inhomogeneous and narrowing mixing scenarios, respectively. While homogeneous mixing is the predominant scenario, leading to a general increase in d_r after mixing, this increase becomes weaker as the cloud matures due to the increased inhomogeneous mixing frequency (Fig. 6c).

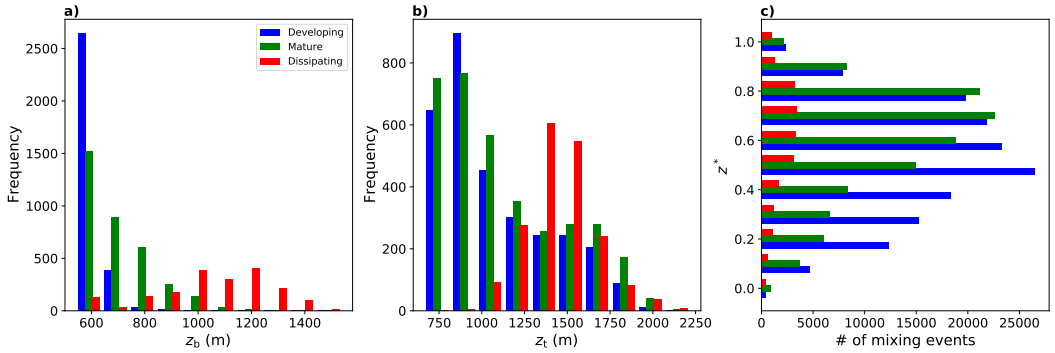

Figure 7. Distributions of a) cloud base height (z_b), b) cloud top height (z_t) and c) number of mixing events in normalized cloud depth (z^*). The colors of the bar indicate different cloud life stages (blue: developing, green: mature, and red: dissipating). All data are obtained from the control case.

4 Vertical Profiles

Shallow cumulus clouds exhibit a range of different cloud base and top heights. A developing cloud does not always extend across the entire cloud layer. Similarly, dissipating clouds dissociate from their base (Zhao & Austin, 2005). Figure 7a and b depict that the cloud base (z_b) and top height (z_t) increase over the cloud life cycle. This indicates that the actual vertical location where the cloud interacts with its surrounding environment also changes over the cloud life cycle. Thus, the vertical distribution of $MSRF_X$ and other properties in normalized cloud depth,

$$z^* = \frac{z - z_b}{z_t - z_b}, \tag{6}$$

is used instead of a vertical profile in the following section. By using z_t and z_b of each individual cloud, z^* is binned into intervals of 0.1 ranging from $z^* = 0$ to 1.

4.1 Mixing Scenario Relative Frequency Profile

Figure 8 shows the vertical distribution of $MSRF_X$ for the control case (Fig. 8e) and the deviations from it in all other simulated cases (denoted as $\Delta MSRF_X$), which are obtained by subtracting the control case $MSRF_X$ profile from the $MSRF_X$ profile of the considered cases. The $MSRF_X$ profiles are determined by estimating the relative frequency of each mixing scenario within each z^* bin. In the control case profile, homogeneous mixing is the predominant scenario in the developing stage (Fig. 8e), in agreement with the volume-averaged results (Fig. 4), especially at $z^* > 0.3$ where mixing is most frequent (Fig. 7c).

In the mature and dissipating stage, homogeneous mixing gradually decreases, especially near the cloud top, while it becomes more frequent near the cloud base. This decrease in the $MSRF_H$ at the cloud top is associated with an increase in $MSRF_I$. In contrast, the increase in $MSRF_H$ at the cloud base is related to a decrease in the $MSRF_N$ (Fig. 8e).

To relate $MSRF_X$ profile changes to mixing relevant properties, we show profiles of these properties averaged among individual clouds for different life stages, in-cloud, and the environmental shell around the cloud (Fig. 9). Environmental shell values are obtained from the first horizontally adjacent grid boxes outside the cloud, constituting a potential source of entrained air. Each profile is cloud area-weight averaged, considering the vertical distribution of cloud area across normalized height. In addition, mixing region profiles averaged over the regions where IHMDs are estimated are also shown. For the mixing region profiles, values before and after the mixing state are averaged, while other profiles show instantaneous values. We note that values at $z^* > 0.9$ in Fig. 9 tend to be affected by the cloud top over-

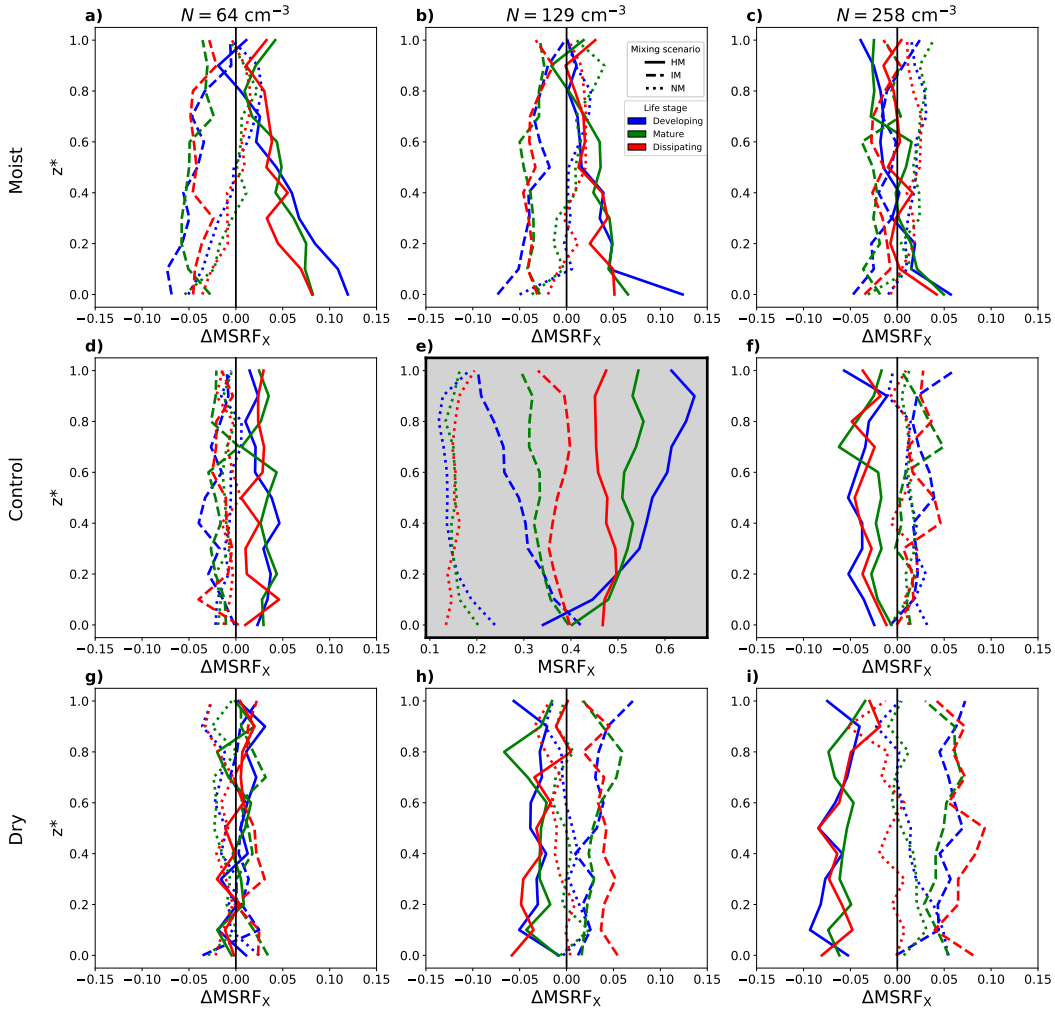

Figure 8. The central panel (e) shows the vertical distribution of mixing scenario relative frequency ($MSRF_X$) for N_a = 129 cm^{-3} under control boundary layer moisture conditions. Surrounding panels illustrate $\Delta MSRF_X$, derived by subtracting the control case $MSRF_X$ profile from the $MSRF_X$ profiles of each specific case. Columns are arranged by aerosol concentration: N_a = 64 cm^{-3} (first), N_a = 129 cm^{-3} (second), and N_a = 258 cm^{-3} (third). Rows indicate the initial boundary layer conditions: moist (top), control (middle), and dry (bottom). Varying line styles represent distinct mixing scenarios—solid for homogeneous (HM), dashed for inhomogeneous (IM), and dotted for narrowing mixing (NM) scenarios. Different cloud life stages are indicated by color: blue (developing), green (mature), and red (dissipating).

shooting the inversion height (~ 1500 m in the simulated BOMEX case), and should be interpreted with care.

The ε profiles (Fig. 9a) show higher values inside the cloud than the environment, and its maximum is near the cloud top in every life stage, as observed by Gerber et al. (2008). High in-cloud ε at the cloud top indicates a shorter τ_{mix} in this region, which explains the high $\mathrm{MSRF_H}$ near the cloud top (Fig. 8e). In the mixing region, ε also increases with height, but the values are lower than in the in-cloud region. This is because the mixture of less turbulent environmental air and potentially more turbulent cloudy air results in an intermediate ε in the mixing region. As the cloud ages, ε decreases at the cloud top, and the $\mathrm{MSRF_H}$ in this region decreases accordingly (Fig. 8e). Below the cloud top, on the other hand, ε and accordingly $\mathrm{MSRF_H}$ slightly increase over the cloud life cycle (Fig. 9a).

While in-cloud N_{c} decreases with height and over the cloud life cycle as expected, N_{c} in the mixing region at $z^* > 0.5$ increases over time, (Fig. 9b). This indicates that the mixing and in-cloud regions of the cloud become less distinct as the cloud ages, i.e., mixing potentially affects a larger fraction of the cloud. Similarly, r_{m} and d_{r} in the mixing region approach their in-cloud values as the cloud ages, supporting this idea (Fig. 9c and d).

It is expected that r_{m} increases with height in all life stages (Fig. 9c). Over the cloud life cycle, r_{m} increases at the cloud base and decreases near the cloud top, while the overall changes are insubstantial. This is because the cloud base elevates over the cloud life cycle (cf. Fig. 7a). The correspondingly larger droplets enable higher $\mathrm{MSRF_H}$ and less $\mathrm{MSRF_N}$ at the cloud base as the cloud ages (cf. Fig. 8e).

While $\overline{S}$ slightly decreases with height and over the cloud life cycle (Fig. 9e), σ_S substantially increases (Fig. 9f). When σ_S is high enough, even high ε at the cloud top might not be able to homogenize the supersaturation field. However, when σ_S is rather low (e.g., $\sigma_S < 0.01$), and $\overline{S}$ and ε are sufficiently large (e.g., at the cloud top in the developing stage) homogeneous mixing dominates (Fig. 8e).

Except for $\overline{S}$, environmental properties change negligible with cloud life stages compared to in-cloud properties (see dashed lines in Fig. 9e). Changes in environmental $\overline{S}$ are mainly due to the aforementioned elevated position of the cloud (cf. Fig. 4), where $\overline{S}$ is lower (Fig. S4e). This implies that drier entrained air also stimulates the lower σ_S as the cloud ages. Thus, considering changes in the vertical location of clouds over time is an important factor in evaluating the life cycle evolution of shallow cumulus cloud mixing characteristics.

The complex interplay between vertical profiles of variables shown in Fig. 9 affecting $\mathrm{MSRF_X}$ underscores the need for a variable that contains more comprehensive meaning. Thus, we estimate the transition length scale $l^* = \varepsilon^{\frac{1}{2}} \tau_{\mathrm{evp}}{}^{\frac{3}{2}}$ (Baker et al., 1980b; Lehmann et al., 2009), which indicates the length scale where Damköhler number becomes 1, separating homogeneous and inhomogeneous mixing. Accordingly, smaller l^* indicate more potential for inhomogeneous mixing. To estimate l^*, we first estimate τ_{evp} (Fig. 9g) using profiles of r_{m} (Fig. 9c) and $\overline{S_{\mathrm{neg.}}}$ (not shown) to predict the entrained S for the in-cloud and mixing regions.

τ_{evp} generally decreases over the cloud life cycle due to the strong decrease in $\overline{S}$ which overruns the increase in r_{m}. As ε increases less than τ_{evp} decreases (Fig. 9a and g), l^* decreases over the cloud life cycle, indicating more potential for inhomogeneous mixing (Fig. 9h). This implies that the life cycle mixing scenario evolution is driven by S affecting τ_{evp}.

We should note that the small l^* at the cloud top does not necessarily indicate more inhomogeneous mixing in this region. The vertical distribution of $\mathrm{MSRF_X}$ does not consider the absolute number of mixing events, and vertical profiles of variables do not capture the variance in each mixing event. Nonetheless, the general pattern in $\mathrm{MSRF_X}$ changes, especially near the cloud top where the mixing events are dominant (Fig. 7c), aligns well with life cycle changes in $\mathrm{MSRF_X}$ in the total cloud volume.

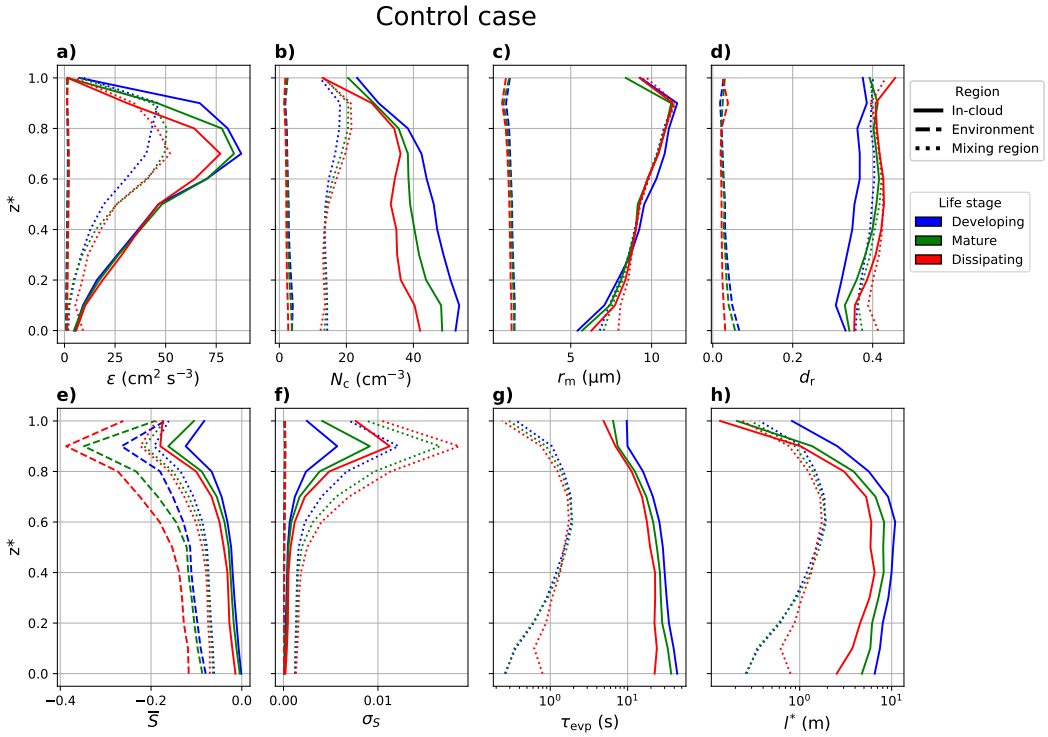

Figure 9. Vertical profiles of a) dissipation rate (ε) b) cloud droplet number concentration (N_c), c) mean droplet radius (r_m), d) droplet radius relative dispersion (d_r), e) mean S ($\overline{S}$), and f) standard deviation of S (σ_S). The line style depicts the region where each variable is averaged (solid: in-cloud, dashed: environment, and dotted: mixing region). Vertical profiles of in-cloud g) evaporation time scale (τ_{evp}) and h) transition length scale (l^*) are also shown. The line colors indicate different cloud life stages (blue: developing, green: mature, and red: dissipating)

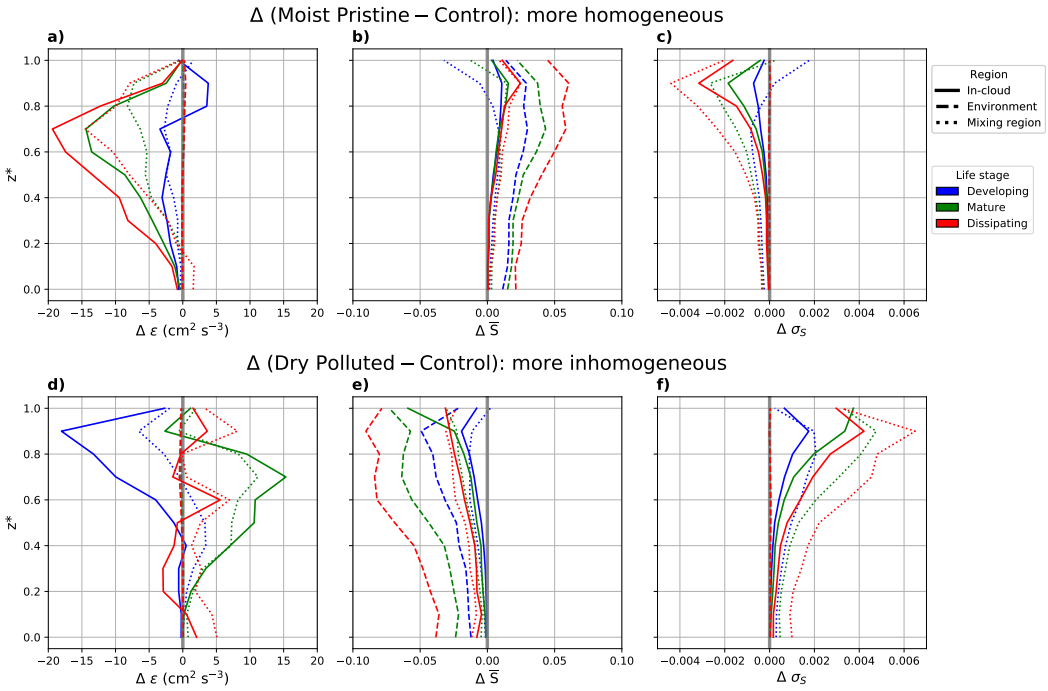

Figure 10. Vertical distribution of the difference between the moist-pristine case and the control case (a, b, and c) and between dry-polluted case and the control case (d, e, and f) for the dissipation rate (1st column), mean supersaturation (2nd column) and supersaturation standard deviation (3rd column). The line colors indicate different cloud life stages (blue: developing, green: mature, and red: dissipating), and the line style depicts the region where each variable is averaged (solid: in-cloud, dashed: environment, and dotted: mixing region). The gray solid line denotes no difference, $\Delta = 0$.

4.2 Microphysical versus Environmental Factors Determining Mixing Scenarios

We have shown that changes in σ_S, $\overline{S}$, ε, and r_m play crucial roles in determining how mixing scenarios change over the cloud life cycle. The following section will discuss these scenarios under varied environmental conditions.

Overall, $\Delta\mathrm{MSRF_X}$ profiles are uniform, suggesting a consistent change in vertical $\mathrm{MSRF_X}$ profiles while values differ (Fig. 8), confirming results shown in Fig. 4. The homogeneous mixing scenario occurs more frequently in moister boundary layers (Fig. 8b) and pristine environments (Fig. 8d) than in the control case. On the other hand, the inhomogeneous mixing scenario is more frequent in drier boundary layers (Fig. 8h) and for higher aerosol concentrations (Fig. 8f).

To compare the changes in the properties affecting entrainment and mixing, we pick a *more homogeneous case* ($N_\mathrm{a} = 64$ cm^{-3} and moister boundary layer, referred to as "moist pristine" in Fig. 10a, b and c), and a *more inhomogeneous case* ($N_\mathrm{a} = 258$ cm^{-3} and drier boundary layer, referred to as "dry polluted" in Fig. 10d, e and f).

Results from the *more homogeneous case* show larger $\overline{S}$ and smaller σ_S (Fig. 10b and c), although ε is lower (Fig. 10a). Likewise, a moister boundary layer with the same aerosol concentration shows more homogeneous mixing (Fig. 8b) due to a higher $\overline{S}$ and lower σ_S (Fig. S5e and f), while ε is lower (Fig. S5a).

The *more inhomogeneous case* shows the opposite trend to the *more homogeneous case* showing smaller $\overline{S}$ and larger σ_S, regardless of ε (Fig. 10d, e, and f). This is consistent in a drier boundary layer with the same aerosol concentration, while other variables are largely unchanged (Fig. S6e and f), implying that the changes in $\overline{S}$ and σ_S are a stronger indicator in determining the predominant mixing type than ε.

Interestingly, homogeneous and inhomogeneous $\Delta\mathrm{MSRF_X}$ profiles in the case with a drier boundary layer (Fig. 8h) closely resemble profiles from a doubling of the aerosol concentrations (Fig. 8f). Similar pairs are shown between the moister boundary layer and halved aerosol concentration cases (Fig. 8b and d) and counteracting cases (Fig. 8c and g). This suggests that the microphysical and environmental properties can have equivalent impacts on mixing scenarios.

However, inhomogeneous mixing is always more frequent in a drier boundary layer (Fig. 8g, h and i). This is because in the drier boundary layers, $\overline{S}$ is lower, and σ_S are higher (Fig. S6), whereas, in the more polluted boundary layer, changes in $\overline{S}$ and σ_S are negligible compared to r_m and N_c change (Fig. S7). Therefore, while the complex interplay between $\overline{S}$, σ_S, r_m and N_c all affects the mixing scenario, $\overline{S}$ and σ_S play the most important role.

The narrowing mixing scenario is more related to the aerosol number concentration. A higher aerosol concentration (258 cm^{-3}), which implies a higher N_c and a smaller r_m, consistently results in a slightly higher $\mathrm{MSRF_N}$s than in the control case. This remains true even in moist boundary layers where homogeneous mixing is more prevalent (Fig. 8c, f, and i). On the other hand, for lower aerosol concentrations (64 cm^{-3}), narrowing mixing is always less frequent regardless of the boundary layer humidity due to the correspondingly larger droplets (Fig. 8a, d, and g). Thus, the narrowing mixing scenario is less dependent on the environmental properties than homogeneous and inhomogeneous mixing scenarios and is primarily related to the prevalence of small droplets in DSD, as outlined in Lim and Hoffmann (2023).

5 Discussions and Conclusions

Unraveling the intricate yet crucial process of entrainment and mixing is essential for understanding clouds and their influence on the climate due to their significant influence on the radiation budget and precipitation formation. However, key questions remain regarding

the prevalence and variability of distinct mixing scenarios in space and time. Therefore, it is important to understand the relationship between different mixing scenarios and the environmental and microphysical factors determining them. In this study, we use a large eddy simulation (LES) model coupled with a Lagrangian cloud model (LCM) and a linear eddy model (LEM), the L^3 model, to simulate maritime shallow cumulus clouds, classifying them into different life stages and analyzing the evolution of mixing scenarios under varying environmental conditions.

The key insights of this paper are:

- While different mixing scenarios occur concurrently, we confirm the evolution from a homogeneous mixing-dominant phase to a more inhomogeneous mixing phase over the cloud life cycle, irrespective of initial boundary layer humidity and aerosol concentration.
- In most cases, homogeneous mixing is dominant, but inhomogeneous mixing can prevail in the dissipating stages of shallow cumuli in drier and more polluted boundary layers.
- The mean ($\overline{S}$) and standard deviation (σ_S) of in-cloud supersaturation S encapsulate the evolution from homogeneous to inhomogeneous mixing and the vertical distribution of mixing scenarios. The values of the mean and standard deviation of S are changed either due to the accumulated effects of entrainment and mixing events or by the clouds shifting upward in the dissipating stage.

In summary, this study expands the understanding from previously observed increasingly inhomogeneous mixing in diluted clouds (e.g., Lehmann et al., 2009; Schmeissner et al., 2015) by suggesting $\overline{S}$ as a useful parameter to estimate mixing scenarios without more complex measures, based on the high correlation between $\overline{S}$ and σ_S. Less diluted developing clouds with higher dissipation rates indicate faster homogenization and lower σ_S. Higher $\overline{S}$ in these clouds imply slower droplet evaporation, making homogeneous mixing more favorable. Over the cloud life cycle, dilution causes entrained air to accumulate inside the cloud without completely saturating. Thus, in the dissipating stage, clouds have higher σ_S and lower $\overline{S}$, making the homogenization take longer, enabling more inhomogeneous mixing.

The narrowing mixing scenario (Lim & Hoffmann, 2023) is more dependent on the abundance of small droplets than $\overline{S}$ and σ_S. This confirms that the narrowing mixing scenario is not a part of homogeneous or inhomogeneous mixing but only depends on the availability of small droplets, providing ample opportunities for complete evaporation (Lim & Hoffmann, 2023).

In conclusion, our findings highlight the need for in-depth consideration of supersaturation fluctuations and mixing scenarios, as cumulus clouds cannot be characterized by one single mixing scenario. As inhomogeneous mixing becomes more dominant in drier and more polluted environments, its impact can alter in a changing climate. Further studies could determine these relationships across different cloud types, such as in stratocumulus, where recent observation showed that homogeneous mixing is more frequent in the moister environment (Yeom et al., 2023), aligning with the results shown in this paper. Moreover, investigating how inhomogeneous mixing changes the cloud life cycle will deepen our understanding of the effects of different mixing scenarios on cloud dynamics and their climate implications.

Open Research

Simulation results for this research are available in Lim (2023). The System for Atmospheric Modeling (SAM) code is available under the link http://rossby.msrc.sunysb.edu/SAM.html, with permission from its developer, Dr. M. Khairoutdinov (Khairoutdinov & Randall, 2003). Figures are made with Matplotlib version 3.3.4, available under the link https://matplotlib.org/.

K-means clustering and multiple-linear regression analysis are done with Scikit-learn: Machine Learning in Python (Pedregosa et al., 2011).

Acknowledgments

This work is supported by the Emmy-Noether program of the German Research Foundation (DFG) under grant HO 6588/1-1. The authors gratefully acknowledge the Gauss Centre for Supercomputing e.V. (www.gauss-centre.eu) for funding this project by providing computing time on the GCS Supercomputer SuperMUC-NG at Leibniz Supercomputing Centre (www.lrz.de).

References

Andrejczuk, M., Grabowski, W. W., Malinowski, S. P., & Smolarkiewicz, P. K. (2006). Numerical simulation of cloud–clear air interfacial mixing: Effects on cloud microphysics. *Journal of the atmospheric sciences*, *63*(12), 3204–3225. doi: 10.1175/JAS3813.1

Baker, M., Corbin, R., & Latham, J. (1980a). The influence of entrainment on the evolution of cloud droplet spectra: I. a model of inhomogeneous mixing. *Quarterly Journal of the Royal Meteorological Society*, *106*(449), 581-598. doi: 10.1002/qj.49710644914

Baker, M., Corbin, R., & Latham, J. (1980b). The influence of entrainment on the evolution of cloud droplet spectra: I. a model of inhomogeneous mixing. *Quarterly Journal of the Royal Meteorological Society*, *106*(449), 581–598. doi: 10.1002/qj.49710644914

Baker, M., & Latham, J. (1979). The evolution of droplet spectra and the rate of production of embryonic raindrops in small cumulus clouds. *Journal of the Atmospheric Sciences*, *36*(8), 1612–1615. doi: 10.1175/1520-0469(1979)036\%3C1612:TEODSA\%3E2.0.CO;2

Blyth, A. M. (1993). Entrainment in cumulus clouds. *Journal of Applied Meteorology and Climatology*, *32*(4), 626-641. doi: 10.1175/1520-0450(1993)032<0626:EICC>2.0.CO;2

Boucher, O., Randall, D., Artaxo, P., Bretherton, C., Feingold, G., Forster, P., ... others (2013). Clouds and aerosols. In *Climate change 2013: The physical science basis. contribution of working group i to the fifth assessment report of the intergovernmental panel on climate change* (pp. 571–657). Cambridge University Press.

Burnet, F., & Brenguier, J.-L. (2007). Observational study of the entrainment-mixing process in warm convective clouds. *Journal of the atmospheric sciences*, *64*(6), 1995–2011.

Chandrakar, K. K., Grabowski, W. W., Morrison, H., & Bryan, G. H. (2021). Impact of entrainment mixing and turbulent fluctuations on droplet size distributions in a cumulus cloud: An investigation using lagrangian microphysics with a subgrid-scale model. *Journal of the Atmospheric Sciences*, *78*(9), 2983–3005.

Chen, J., Liu, Y., & Zhang, M. (2020). Effects of lateral entrainment mixing with entrained aerosols on cloud microphysics. *Geophysical Research Letters*, *47*(13), e2020GL087667.

Chosson, F., Brenguier, J.-L., & Schüller, L. (2007). Entrainment-mixing and radiative transfer simulation in boundary layer clouds. *Journal of the atmospheric sciences*, *64*(7), 2670–2682.

Derksen, J., Roelofs, G.-J., & Röckmann, T. (2009). Influence of entrainment of ccn on microphysical properties of warm cumulus. *Atmospheric chemistry and physics*, *9*(16), 6005–6015.

Desai, N., Liu, Y., Glienke, S., Shaw, R. A., Lu, C., Wang, J., & Gao, S. (2021). Vertical variation of turbulent entrainment mixing processes in marine stratocumulus clouds using high-resolution digital holography. *Journal of Geophysical Research: Atmospheres*, *126*(7), e2020JD033527.

Drueke, S., Kirshbaum, D. J., & Kollias, P. (2020). Environmental sensitivities of shallow-cumulus dilution–part 1: Selected thermodynamic conditions. *Atmospheric Chemistry*

and Physics, *20*(21), 13217–13239.
Eytan, E., Koren, I., Altaratz, O., Pinsky, M., & Khain, A. (2021). Revisiting adiabatic fraction estimations in cumulus clouds: high-resolution simulations with a passive tracer. *Atmospheric chemistry and physics*, *21*(21), 16203–16217.
Forster, P., Storelvmo, T., Armour, K., Collins, W., Dufresne, J.-L., Frame, D., ... others (2021). The earth's energy budget, climate feedbacks, and climate sensitivity.
Gao, S., Lu, C., Liu, Y., Yum, S. S., Zhu, J., Zhu, L., ... Wu, S. (2021). Comprehensive quantification of height dependence of entrainment mixing between stratiform cloud top and environment. *Atmospheric Chemistry and Physics*, *21*(14), 11225–11241.
Gerber, E., Hermann, M. FRICK, G., B. JENSEN, J., & G. HUDSON, J. (2008). Entrainment, mixing, and microphysics in trade-wind cumulus. *Journal of the Meteorological Society of Japan*, *86*, 87–106.
Grinnell, S. A., Bretherton, C. S., Fraser, A. M., & Stevens, D. E. (1996). Vertical mass flux calculations in hawaiian trade cumulus clouds from dual-doppler radar. *Journal of Atmospheric Sciences*, *53*(13), 1870–1886.
Heus, T., Jonker, H. J., Van den Akker, H. E., Griffith, E. J., Koutek, M., & Post, F. H. (2009). A statistical approach to the life cycle analysis of cumulus clouds selected in a virtual reality environment. *Journal of Geophysical Research: Atmospheres*, *114*(D6).
Hill, A. A., Feingold, G., & Jiang, H. (2009). The influence of entrainment and mixing assumption on aerosol–cloud interactions in marine stratocumulus. *Journal of the Atmospheric Sciences*, *66*(5), 1450–1464.
Hoffmann, F. (2023). The small-scale mixing of clouds with their environment: Impacts on micro-and macroscale cloud properties.
Hoffmann, F., & Feingold, G. (2019). Entrainment and mixing in stratocumulus: Effects of a new explicit subgrid-scale scheme for large-eddy simulations with particle-based microphysics. *Journal of the Atmospheric Sciences*, *76*(7), 1955–1973. doi: 10.1175/JAS-D-18-0318.1
Hoffmann, F., Yamaguchi, T., & Feingold, G. (2019). Inhomogeneous mixing in lagrangian cloud models: Effects on the production of precipitation embryos. *Journal of the Atmospheric Sciences*, *76*(1), 113–133. doi: 10.1175/JAS-D-18-0087.1
Jarecka, D., Grabowski, W. W., Morrison, H., & Pawlowska, H. (2013). Homogeneity of the subgrid-scale turbulent mixing in large-eddy simulation of shallow convection. *Journal of the atmospheric sciences*, *70*(9), 2751–2767.
Katzwinkel, J., Siebert, H., Heus, T., & Shaw, R. A. (2014). Measurements of turbulent mixing and subsiding shells in trade wind cumuli. *Journal of the Atmospheric Sciences*, *71*(8), 2810–2822.
Kerstein, A. R. (1988). A linear-eddy model of turbulent scalar transport and mixing. *Combustion Science and Technology*, *60*(4-6), 391–421. doi: 10.1080/00102208808923995
Khairoutdinov, M. F., & Randall, D. A. (2003). Cloud resolving modeling of the arm summer 1997 iop: Model formulation, results, uncertainties, and sensitivities. *J. Atmos. Sci.*, *60*(4), 607–625. doi: 10.1175/1520-0469(2003)060\%3C0607:CRMOTA\%3E2.0.CO;2
Krueger, S. K., Schlueter, H., & Lehr, P. (2008). Fine-scale modeling of entrainment and mixing of cloudy and clear air. In *15th international conference on clouds and precipitation, cancun, mexico.*
Krueger, S. K., Su, C.-W., & McMurtry, P. A. (1997). Modeling entrainment and finescale mixing in cumulus clouds. *Journal of the atmospheric sciences*, *54*(23), 2697-2712. doi: 10.1175/1520-0469(1997)054<2697:MEAFMI>2.0.CO;2
Lehmann, K., Siebert, H., & Shaw, R. A. (2009). Homogeneous and inhomogeneous mixing in cumulus clouds: Dependence on local turbulence structure. *Journal of the Atmospheric Sciences*, *66*(12), 3641–3659. doi: 10.1175/2009JAS3012.1
Lim, J.-S. (2023, November). *Sam_bomex_output.* Zenodo. Retrieved from `https://doi.org/10.5281/zenodo.10211789` doi: 10.5281/zenodo.10211789
Lim, J.-S., & Hoffmann, F. (2023). Between broadening and narrowing: How mixing affects

the width of the droplet size distribution. *Journal of Geophysical Research: Atmospheres*, *128*(8), e2022JD037900.

Liu, Y., Yau, M.-K., Shima, S.-i., Lu, C., & Chen, S. (2023). Parameterization and explicit modeling of cloud microphysics: Approaches, challenges, and future directions. *Advances in Atmospheric Sciences*, *40*(5), 747–790.

Luo, S., Lu, C., Liu, Y., Bian, J., Gao, W., Li, J., ... Guo, X. (2020). Parameterizations of entrainment-mixing mechanisms and their effects on cloud droplet spectral width based on numerical simulations. *Journal of Geophysical Research: Atmospheres*, *125*(22), e2020JD032972.

Luo, S., Lu, C., Liu, Y., Gao, W., Zhu, L., Xu, X., ... Guo, X. (2021). Consideration of initial cloud droplet size distribution shapes in quantifying different entrainment-mixing mechanisms. *Journal of Geophysical Research: Atmospheres*, *126*(13), e2020JD034455. doi: 10.1029/2020JD034455

Luo, S., Lu, C., Liu, Y., Li, Y., Gao, W., Qiu, Y., ... others (2022). Relationships between cloud droplet spectral relative dispersion and entrainment rate and their impacting factors. *Advances in Atmospheric Sciences*, 1–20. doi: 10.1007/s00376-022-1419-5

McFarlane, S. A., & Grabowski, W. W. (2007). Optical properties of shallow tropical cumuli derived from arm ground-based remote sensing. *Geophysical research letters*, *34*(6).

Morrison, H., & Grabowski, W. W. (2008). Modeling supersaturation and subgrid-scale mixing with two-moment bulk warm microphysics. *Journal of the Atmospheric Sciences*, *65*(3), 792–812. doi: 10.1175/2007JAS2374.1

Neggers, R. A., Jonker, H. J., & Siebesma, A. (2003). Size statistics of cumulus cloud populations in large-eddy simulations. *Journal of the atmospheric sciences*, *60*(8), 1060–1074.

Pedregosa, F., Varoquaux, G., Gramfort, A., Michel, V., Thirion, B., Grisel, O., ... Duchesnay, E. (2011). Scikit-learn: Machine learning in Python. *Journal of Machine Learning Research*, *12*, 2825–2830.

Pinsky, M., Khain, A., Korolev, A., & Magaritz-Ronen, L. (2016). Theoretical investigation of mixing in warm clouds–part 2: Homogeneous mixing. *Atmospheric Chemistry and Physics*, *16*(14), 9255–9272. doi: 10.5194/acp-16-9255-2016

Schmeissner, T., Shaw, R., Ditas, J., Stratmann, F., Wendisch, M., & Siebert, H. (2015). Turbulent mixing in shallow trade wind cumuli: Dependence on cloud life cycle. *Journal of the Atmospheric Sciences*, *72*(4), 1447–1465. doi: 10.1175/JAS-D-14-0230.1

Shima, S.-i., Kusano, K., Kawano, A., Sugiyama, T., & Kawahara, S. (2009). The super-droplet method for the numerical simulation of clouds and precipitation: A particle-based and probabilistic microphysics model coupled with a non-hydrostatic model. *Quarterly Journal of the Royal Meteorological Society: A journal of the atmospheric sciences, applied meteorology and physical oceanography*, *135*(642), 1307–1320. doi: 10.1002/qj.441

Siebesma, A. P., Bretherton, C. S., Brown, A., Chlond, A., Cuxart, J., Duynkerke, P. G., ... others (2003). A large eddy simulation intercomparison study of shallow cumulus convection. *Journal of the Atmospheric Sciences*, *60*(10), 1201–1219.

Slawinska, J., Grabowski, W. W., Pawlowska, H., & Wyszogrodzki, A. A. (2008). Optical properties of shallow convective clouds diagnosed from a bulk-microphysics large-eddy simulation. *Journal of climate*, *21*(7), 1639–1647.

Tölle, M. H., & Krueger, S. K. (2014). Effects of entrainment and mixing on droplet size distributions in warm cumulus clouds. *Journal of Advances in Modeling Earth Systems*, *6*(2), 281–299. doi: 10.1002/2012MS000209

Wang, S., Wang, Q., & Feingold, G. (2003). Turbulence, condensation, and liquid water transport in numerically simulated nonprecipitating stratocumulus clouds. *Journal of the atmospheric sciences*, *60*(2), 262–278.

Witte, M., Chuang, P., & Feingold, G. (2014). On clocks and clouds. *Atmospheric Chemistry and Physics*, *14*(13), 6729–6738.

Xu, X., Lu, C., Liu, Y., Luo, S., Zhou, X., Endo, S., ... Wang, Y. (2022). Influences of an entrainment–mixing parameterization on numerical simulations of cumulus and

stratocumulus clouds. *Atmospheric Chemistry and Physics*, *22*(8), 5459–5475.

Yau, M. K., & Rogers, R. R. (1996). *A short course in cloud physics*. Elsevier.

Yeom, J. M., Szodry, K.-E., Siebert, H., Ehrlich, A., Mellado, J. P., Shaw, R. A., & Yum, S. S. (2023). High-resolution measurements of microphysics and entrainment in marine stratocumulus clouds. *Quarterly Journal of the Royal Meteorological Society*.

Yeom, J. M., Yum, S. S., Shaw, R. A., La, I., Wang, J., Lu, C., ... Matthews, A. (2021). Vertical variations of cloud microphysical relationships in marine stratocumulus clouds observed during the ace-ena campaign. *Journal of Geophysical Research: Atmospheres*, *126*(24), e2021JD034700.

Zhao, M., & Austin, P. H. (2005). Life cycle of numerically simulated shallow cumulus clouds. part i: Transport. *Journal of the atmospheric sciences*, *62*(5), 1269–1290.

Figure 1.

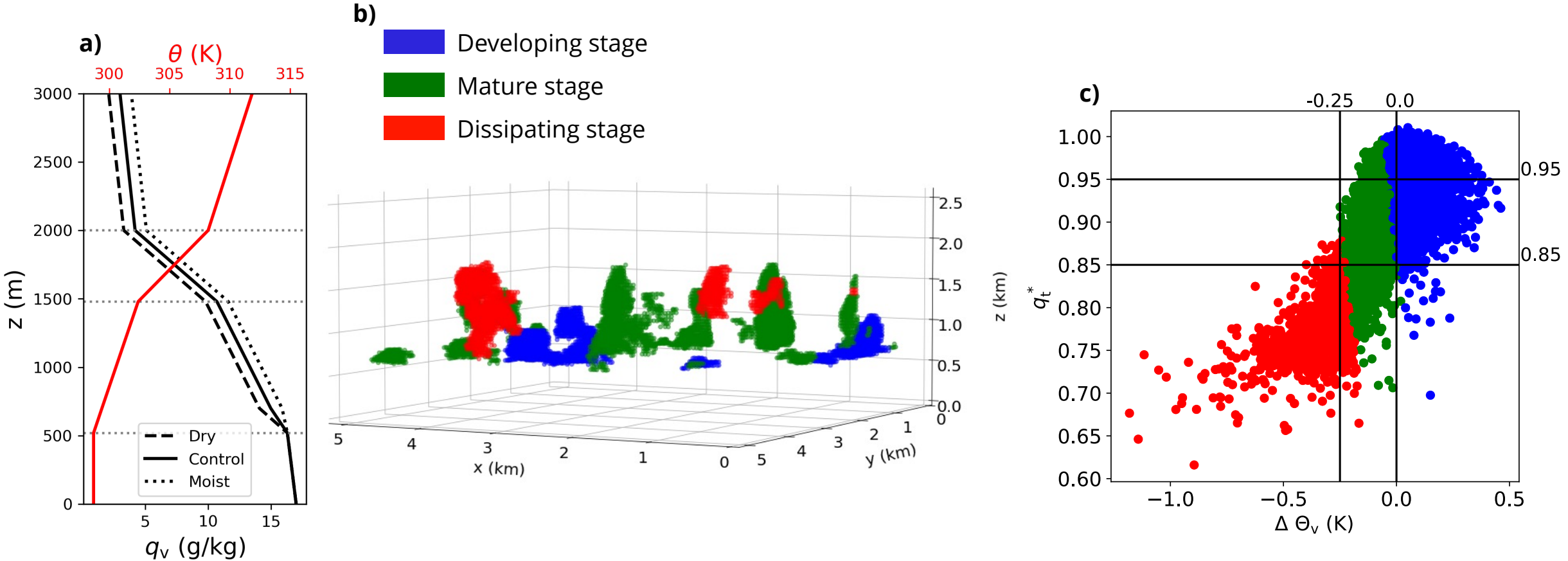
a)
θ (K)
300
305
310
315
3000
2500
2000
1500
1000
500
0
z (m)
Dry
Control
Moist
5
10
15
q_v (g/kg)
b)
Developing stage
Mature stage
Dissipating stage
x (km)
y (km)
z (km)
c)
-0.25
0.0
0.95
0.85
q_t^*
Δ Θ_v (K)

Figure 2.

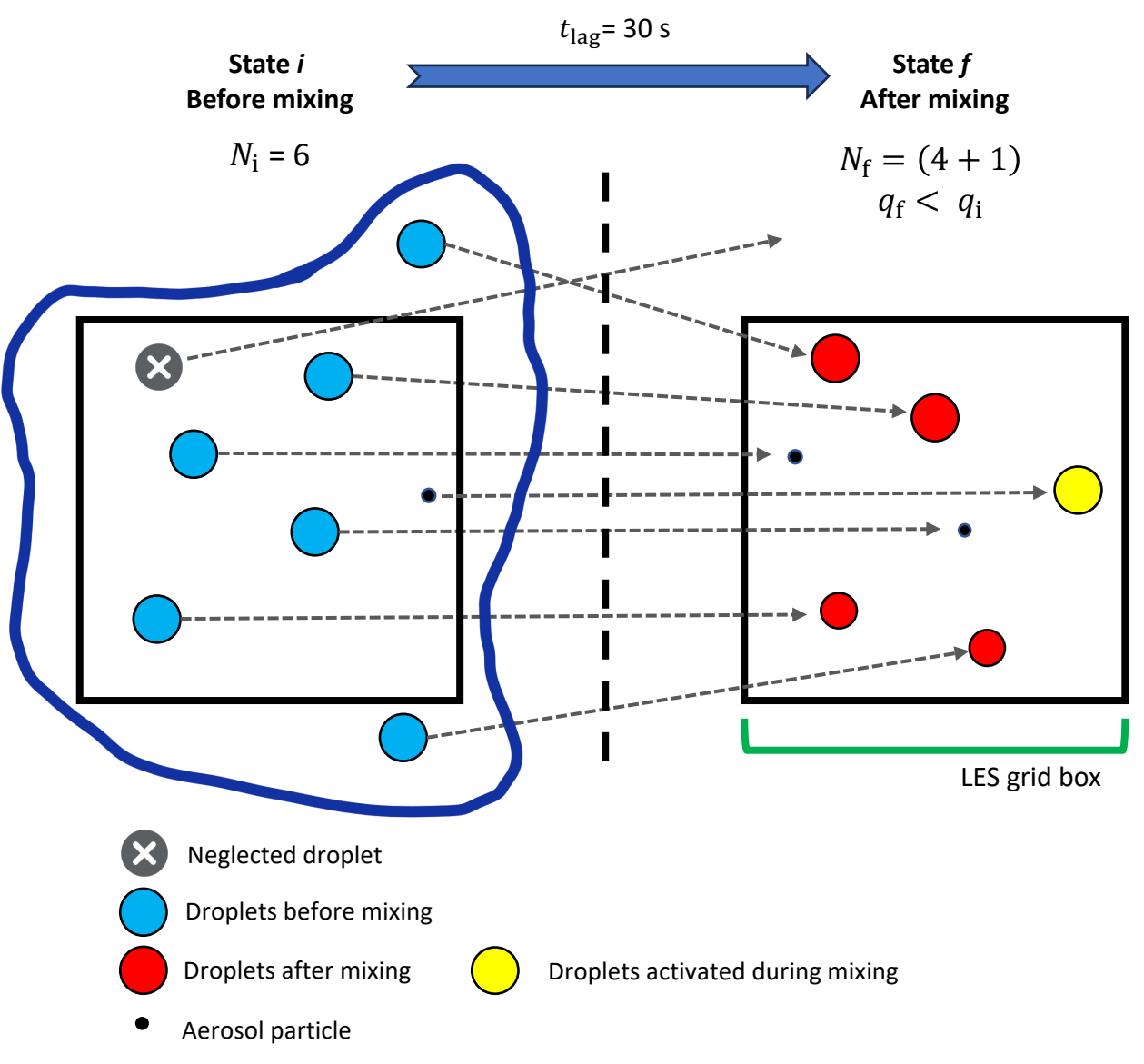
t_{lag}= 30 s
State *i*
Before mixing
State *f*
After mixing
N_i = 6
$N_f = (4 + 1)$
$q_f < q_i$
LES grid box
Neglected droplet
Droplets before mixing
Droplets after mixing
Droplets activated during mixing
Aerosol particle

Figure 3.

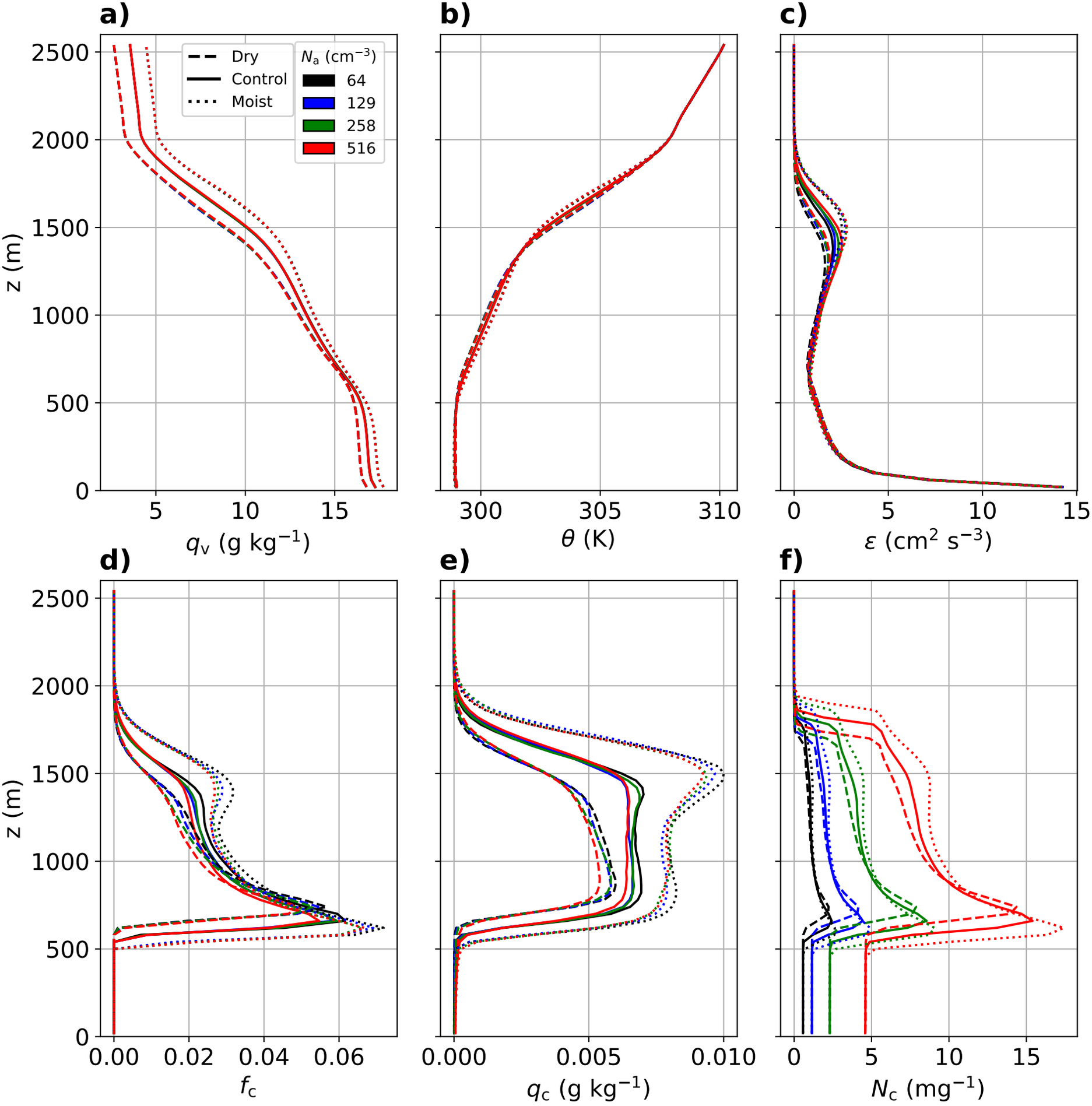
a)
b)
c)
d)
e)
f)
Dry
Control
Moist
N_a (cm^{-3})
64
129
258
516
z (m)
q_v (g kg^{-1})
θ (K)
ε (cm^2 s^{-3})
f_c
q_c (g kg^{-1})
N_c (mg^{-1})

Figure 4.

a)

Homogeneous mixing

Inhomogeneous mixing

Narrowing mixing

$MSRF_X$

1.0
0.8
0.6
0.4
0.2
0.0

Cloud stage
Developing
Mature
Dissipating

b)

Homogeneous mixing

$MSRF_H$

0.60
0.55
0.50
0.45
0.40

Dry
Control
Moist

N_a (cm^{-3})
64
129
258
516

Developing
Mature
Dissipating

c)

Inhomogeneous mixing

$MSRF_I$

0.45
0.40
0.35
0.30
0.25

Developing
Mature
Dissipating

d)

Narrowing mixing

$MSRF_N$

0.16
0.15
0.14
0.13
0.12
0.11

Developing
Mature
Dissipating

Figure 5.

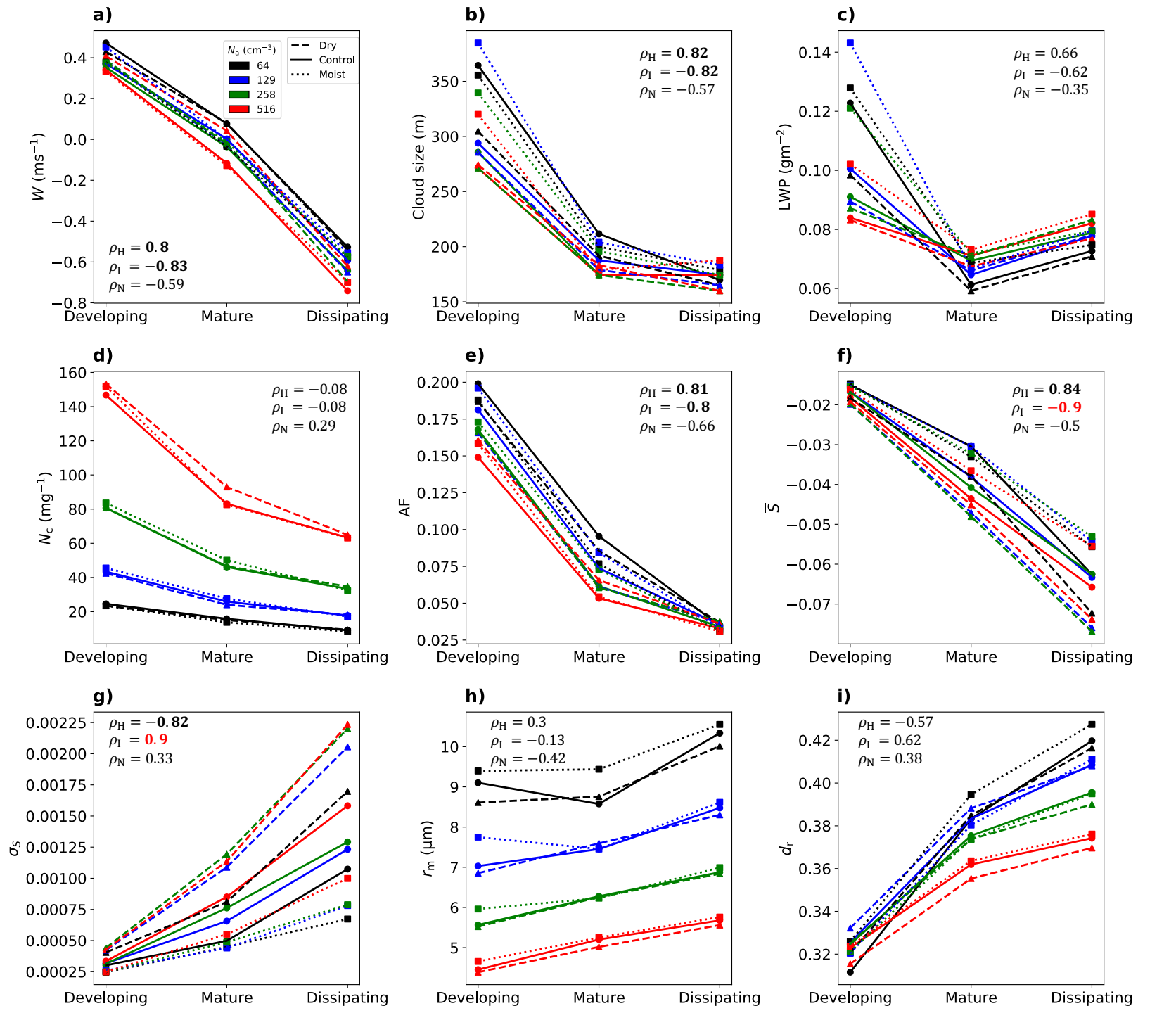
a)
b)
c)
d)
e)
f)
g)
h)
i)
N_a (cm^{-3})
64
129
258
516
Dry
Control
Moist
W (ms^{-1})
$\rho_H = \mathbf{0.8}$
$\rho_I = \mathbf{-0.83}$
$\rho_N = -0.59$
Cloud size (m)
$\rho_H = \mathbf{0.82}$
$\rho_I = \mathbf{-0.82}$
$\rho_N = -0.57$
LWP (gm^{-2})
$\rho_H = 0.66$
$\rho_I = -0.62$
$\rho_N = -0.35$
N_c (mg^{-1})
$\rho_H = -0.08$
$\rho_I = -0.08$
$\rho_N = 0.29$
AF
$\rho_H = \mathbf{0.81}$
$\rho_I = \mathbf{-0.8}$
$\rho_N = -0.66$
$\overline{S}$
$\rho_H = \mathbf{0.84}$
$\rho_I = \mathbf{-0.9}$
$\rho_N = -0.5$
σ_S
$\rho_H = \mathbf{-0.82}$
$\rho_I = \mathbf{0.9}$
$\rho_N = 0.33$
r_m (μm)
$\rho_H = 0.3$
$\rho_I = -0.13$
$\rho_N = -0.42$
d_r
$\rho_H = -0.57$
$\rho_I = 0.62$
$\rho_N = 0.38$
Developing
Mature
Dissipating

Figure 6.

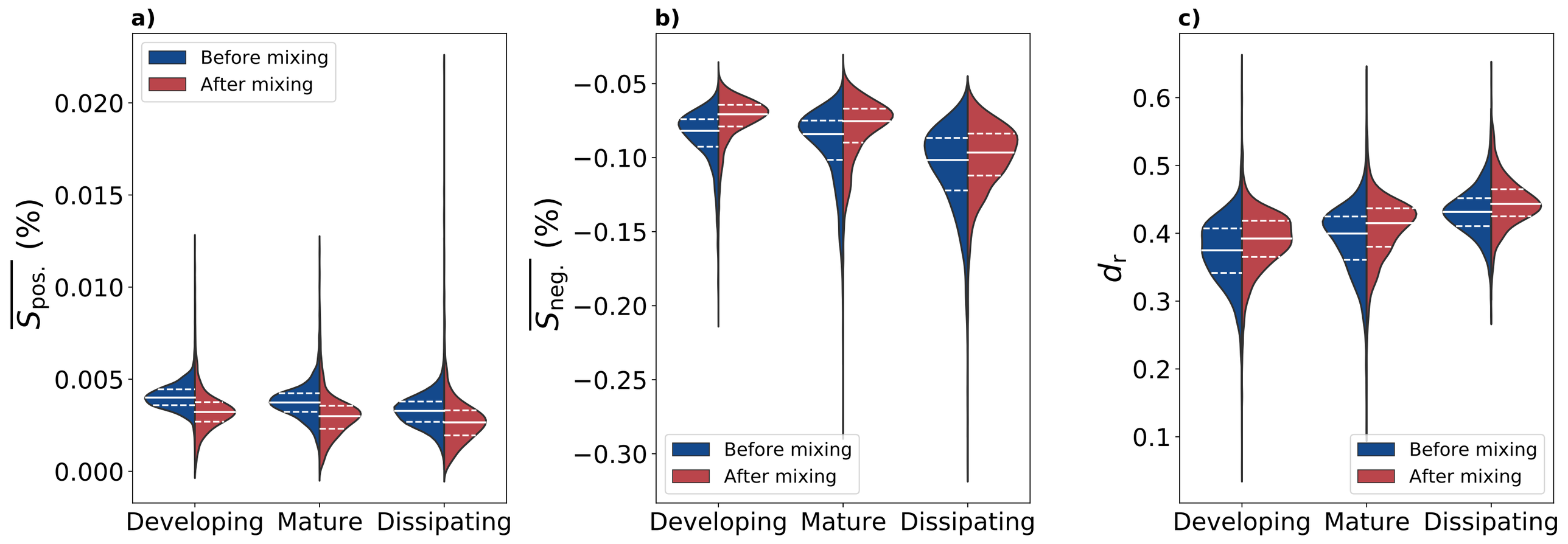
a)
Before mixing
After mixing
0.020
0.015
0.010
0.005
0.000
$\overline{S_{pos.}}$ (%)
Developing
Mature
Dissipating
b)
−0.05
−0.10
−0.15
−0.20
−0.25
−0.30
$\overline{S_{neg.}}$ (%)
Before mixing
After mixing
Developing
Mature
Dissipating
c)
0.6
0.5
0.4
0.3
0.2
0.1
d_r
Before mixing
After mixing
Developing
Mature
Dissipating

Figure 7.

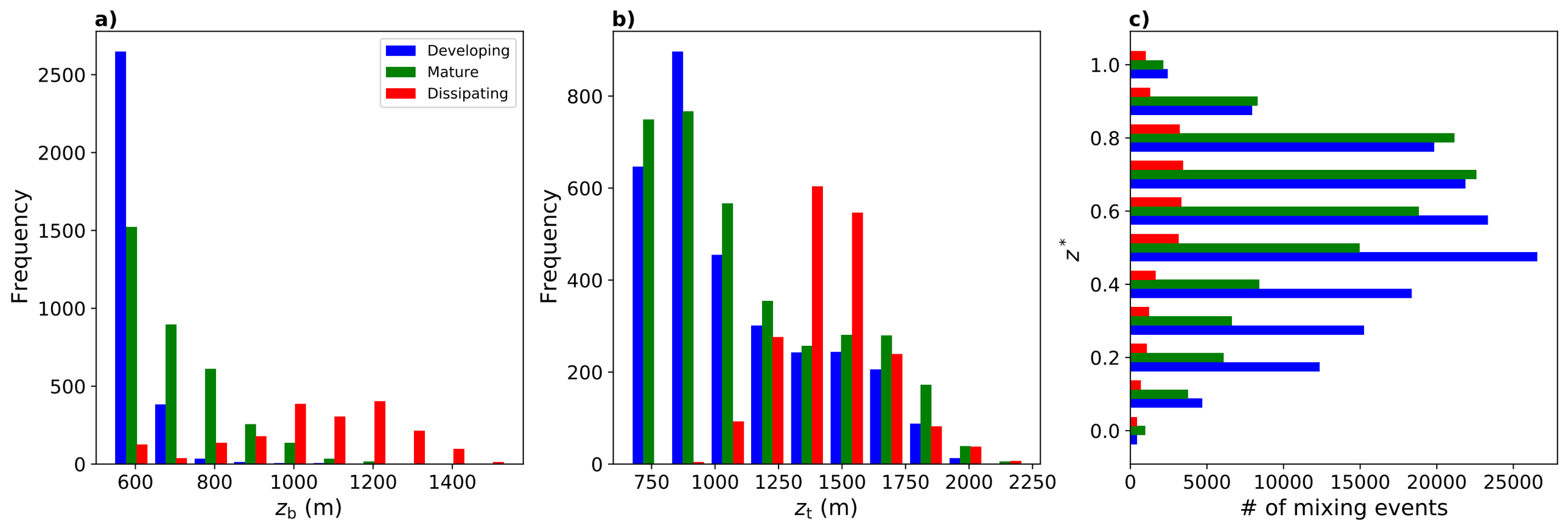
a)
b)
c)
Developing
Mature
Dissipating
Frequency
z_b (m)
z_t (m)
z^*
# of mixing events

Figure 8.

a) $N = 64$ cm^{-3}
b) $N = 129$ cm^{-3}
c) $N = 258$ cm^{-3}
d)
e)
f)
g)
h)
i)
Moist
Control
Dry
z*
$\Delta MSRF_X$
$MSRF_X$
Mixing scenario
HM
IM
NM
Life stage
Developing
Mature
Dissipating

Figure 9.

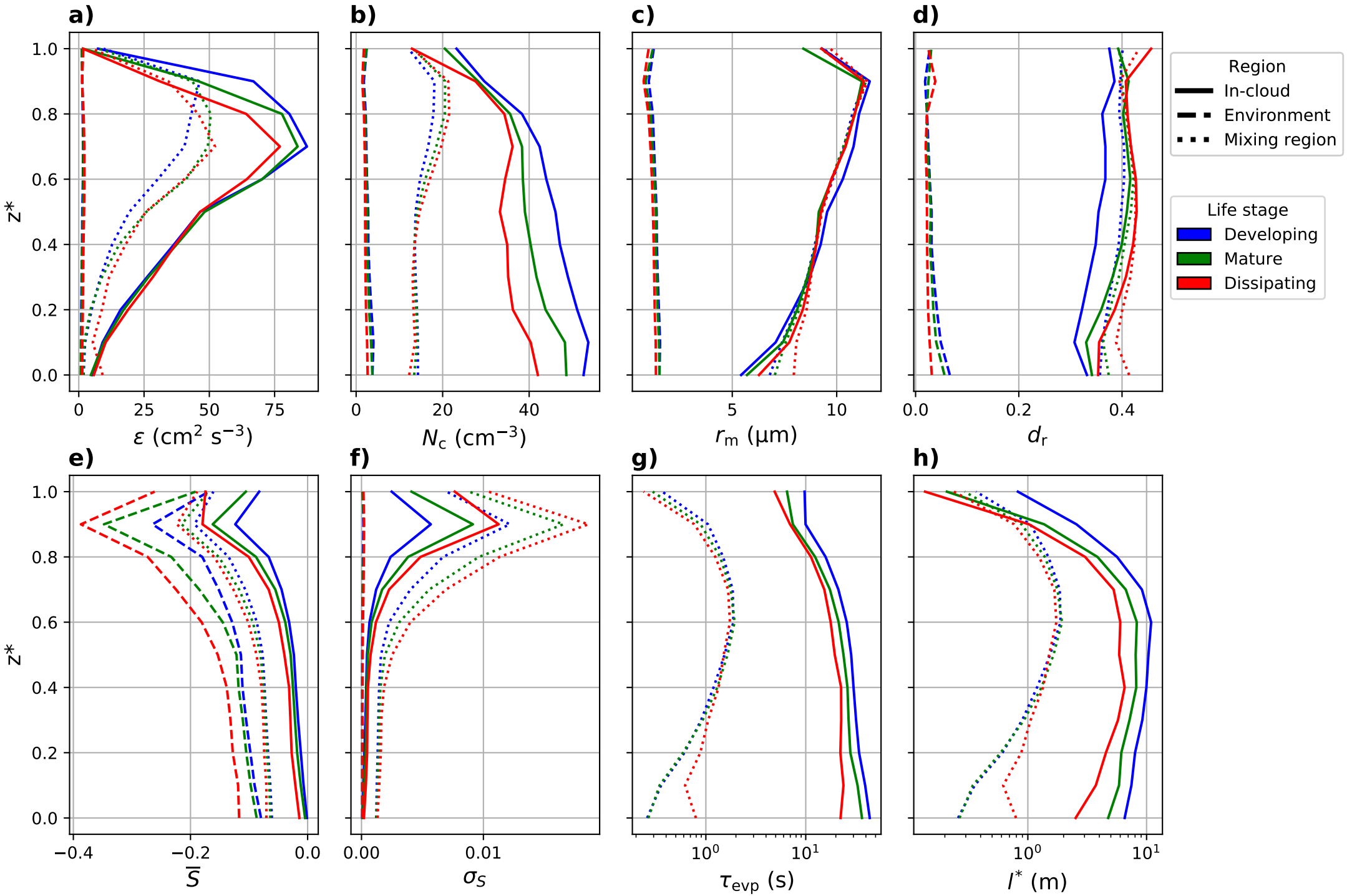
Control case
a)
b)
c)
d)
e)
f)
g)
h)
z*
ε (cm² s⁻³)
N_c (cm⁻³)
r_m (μm)
d_r
S̄
σ_S
τ_evp (s)
l* (m)
Region
In-cloud
Environment
Mixing region
Life stage
Developing
Mature
Dissipating

Figure 10.

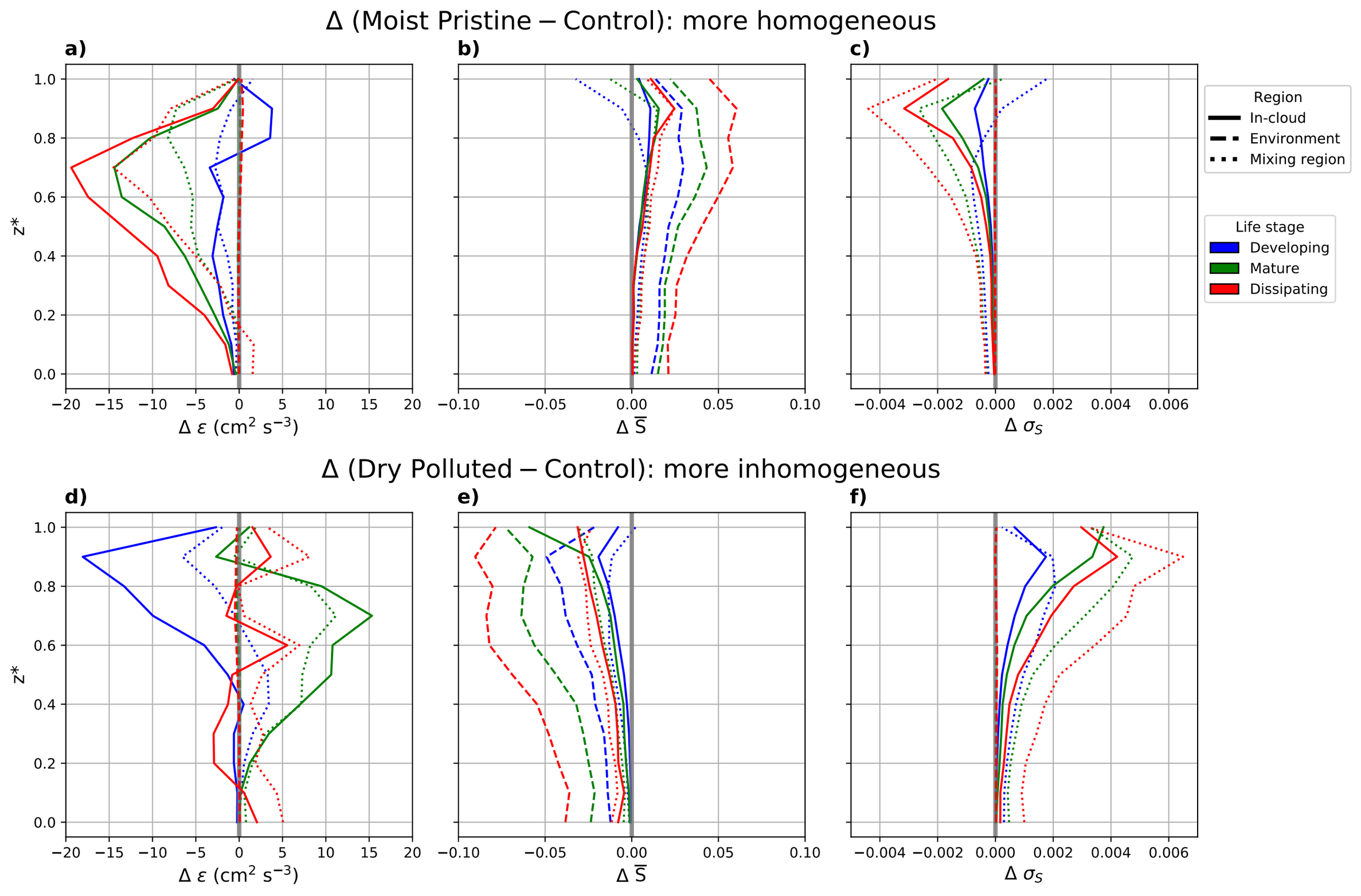
Δ (Moist Pristine − Control): more homogeneous
a)
b)
c)
Region
In-cloud
Environment
Mixing region
Life stage
Developing
Mature
Dissipating
z*
Δ ε (cm² s⁻³)
Δ S̄
Δ σS
Δ (Dry Polluted − Control): more inhomogeneous
d)
e)
f)